Lawrence Berkeley National Laboratory
LBL Publications

Title

Characterization of flow and transport in a fracture network at the EGS Collab field experiment through stochastic modeling of tracer recovery

Permalink
https://escholarship.org/uc/item/2vt256ds

Authors
Wu, Hui
Fu, Pengcheng
Morris, Joseph P
et al.

Publication Date
2021-02-01

DOI
10.1016/j.jhydrol.2020.125888

Peer reviewed

eScholarship.org Powered by the California Digital Library
University of California

Title: Characterization of flow and transport in a fracture network at the EGS Collab field experiment through stochastic modeling of tracer recovery

Author: Hui Wu[1], Pengcheng Fu[1], Joseph P. Morris[1], Earl D. Mattson[2], Ghanashyam Neupane[2], Megan M. Smith[1], Adam J. Hawkins[3,4], Yuran Zhang[3,4], Timothy Kneafsey[5], and the EGS Collab Team

Affiliation:

[1]Atmospheric, Earth, and Energy Division, Lawrence Livermore National Laboratory, Livermore, CA, USA.

[2]Energy Recovery and Sustainability Department, Idaho National Laboratory, Idaho Falls, ID, USA.

[3]Mattson Hydrology, LLC, Victor, ID, USA.

[4]Department of Energy Resources Engineering, Stanford University, Stanford, CA, USA.

[5]TomKat Center for Sustainable Energy, Stanford University, Stanford, CA, USA.

[6]Earth and Environmental Sciences Division, Lawrence Berkeley National Laboratory, Berkeley, CA, USA.

Corresponding author: Pengcheng Fu (fu4@llnl.gov)

Abstract: Energy extraction from subsurface reservoirs is important for addressing the increasing energy demand and environmental concerns such as global warming. However, the characterization of subsurface reservoirs, particularly reservoirs dominated by fracture networks remains a challenge due to the lack of means to directly observe subsurface processes. This study explores the feasibility and efficacy of characterizing fracture flow and transport processes in an enhanced geothermal system (EGS) testbed through stochastic tracer modeling. There are two enabling factors that allow application of stochastic modeling to characterize a subsurface reservoir. First, an abundance of geological and geophysical measurements enables the development of a high-fidelity and well-constrained fracture network model. Second, high-performance computing (HPC) allows running massive realizations efficiently. Six conservative tracer tests were stochastically modeled and produced satisfactory realizations that successfully reproduce field tracer recovery data from each tracer test. The evolution of flow and transport processes in the fracture network was then analyzed from these satisfactory realizations. The present study demonstrates that stochastic tracer modeling on a high-fidelity fracture network model is feasible and can provide important insights regarding flow and transport characteristics in subsurface fractured reservoirs.

Keywords: Fractured reservoirs, characterization, enhanced geothermal system, tracer testing, stochastic modeling.

1. Introduction

Subsurface reservoirs are widely exploited around the world for energy recovery and geological storage of industrial wastes including CO_2. The successful exploitation of a subsurface reservoir requires a comprehensive understanding of flow and transport characteristics in the reservoir, particularly in the context of unconventional oil/gas extraction (Middleton et al., 2015), geothermal heat recovery (Brown et al., 2012; Fu et al., 2016; McClure & Horne, 2014; U.S. Department of Energy, 2019), CO_2 storage (Fu et al., 2017; Sun & Tong, 2017), as well as radioactive and toxic industrial wastes containment (Cuss et al., 2015; Sudicky & Frind, 1984; Sun & Buscheck, 2003; Tang et al., 1981; Tsang et al., 2015). Quantitative characterization of flow and transport processes in subsurface reservoirs is commonly based on flow (or pressure) and tracer tests in conjunction with various geological and geophysical investigations such as core logging, outcrop analysis, and seismic and electrical imaging (Berkowitz, 2002; Goovaerts, 1997; Juliusson & Horne, 2013; Karmakar et al., 2016; Neuman, 2005; Vandenbohede and Lebbe, 2003). The inference of spatially variable hydraulic and transport properties can be achieved by matching the measured flow and tracer data with results from either analytical or numerical models constrained by geophysical investigations (Bullivant & O'Sullivan, 1989; Cacas et al., 1990b; Castagna et al., 2011; Hawkins et al., 2017a, 2017b, 2018; Radilla et al., 2012).

A major difficulty in flow and tracer data interpretation is that the available geological and geophysical data are generally insufficient to eliminate the many uncertainties pertaining to characterizing subsurface reservoirs, especially the complex fracture networks which provide principal pathways for flow and transport processes in many subsurface reservoirs. A common method to accommodate these uncertainties in subsurface analysis is stochastic modeling (Cacas et al., 1990a; Geier et al., 2019; Moreno et al., 1988; Ptak et al., 2004; Tsang et al., 1996), which aims to reproduce flow and tracer measurements from massive randomly generated realizations.

The efficacy of stochastic modeling is often undermined by two major challenges. The first one is the difficulty in developing a high-fidelity and well-constrained model with appropriate reduction in model complexity based on geological and geophysical observations and measurements. An over-simplified stochastic model may not be able to capture the necessary complexity of the field, while a complex stochastic model with a high-dimensional parameter space is prone to overfitting. The second challenge is that numerous realizations are required to sufficiently cover the parameter space of a stochastic model because each parameter pertaining to a subsurface reservoir can vary in a wide range. Most previous efforts either use analytical solutions or simplified numerical models to make stochastic modeling computationally tractable (Bullivant and O'Sullivan, 1989; Hawkins et al., 2017b, 2018; Radilla et al., 2012), or empirically estimate the values of some parameters to reduce the parameter space so that fewer realizations are required (Vogt et al., 2012). For example, to characterize fracture flow in the Soultz-sous-Forêts EGS site, Vogt et al (2012) performed stochastic modeling of field tracer experiments with 10,000 realizations generated from a

Monte Carlo approach, each with a different 3D permeability distribution. However, none of these realizations could match the two measured tracer breakthrough curves (BTCs) simultaneously, indicating that some other complexities relevant to the tracer transport process, such as dispersivity and porosity, may not have been properly accommodated in the stochastic model. Vogt et al. (2012) also suggested that a better fitting quality might have been possible if the realization number had been some orders of magnitude larger.

In the past several decades, increasing subsurface activities and the demand for high-fidelity predictions of subsurface processes have greatly accelerated the development of comprehensive geological/geophysical monitoring techniques and high-performance computing (HPC) capabilities, which provide new opportunities to improve the methodology for subsurface reservoir characterization. With these techniques and capabilities, it is now possible to use the following strategy to address the aforementioned challenges. First, high-quality geological and geophysical data are utilized to improve the understanding of subsurface fracture networks and thereby to rationally define the parameter space for stochastic modeling. For certain data-rich environments, high-fidelity models can be constrained by honoring available field observations and measurements in a holistic manner. Second, HPC capabilities allow a massive number of realizations and enable a thorough sweeping of the parameter space of the developed high-fidelity model.

Following this strategy, the present study explores using stochastic tracer modeling to characterize flow and transport processes in a subsurface fracture network in a data-rich environment with HPC-enhanced modeling power. We use the ongoing EGS Collab project (Kneafsey et al., 2019; Kneafsey et al., 2020) as an example to illustrate the development of a high-fidelity fracture network model from comprehensive geological and geophysical data and use a stochastic approach with massive realizations to simulate the tracer transport process in the fracture network. For this specific site, a stochastic approach is appropriate and necessary for the following reasons: 1) The developed high-fidelity fracture network model has a high-dimensional parameter space and uses randomly-distributed fields (spatial distribution of aperture), which cannot be described using continuous function forms. Deterministic methods such as Bayesian inversion may not be applicable. 2) Even in this data-rich environment, it is still likely that the viable solutions are not unique. Stochastic modeling allows multiple viable solutions to be retrieved, and we can gain insights into the flow and transport characteristics from the commonalities among these solutions.

The paper is organized as follows. Section 2 briefly introduces the EGS Collab experiment testbed, including well configuration, geological and geophysical investigations, hydraulic stimulation activities, and the tracer tests modeled by the current work. In Section 3, based on various geophysical measurements and observations, we develop a fracture network model involving both natural and hydraulic fractures for subsequent stochastic modeling of the tracer tests. We also present the numerical methods for flow and tracer simulation, as well as the details of the stochastic framework. Sections 4 and 5 present modeling results and the corresponding interpretations regarding flow and transport characteristics in the fracture network model. Section 6 demonstrates the consistency between modeling results and additional field observations, analyzes the evolution of flow and transport processes in the fracture network model, and discusses the effect of tracer data quality and quantity on stochastic modeling.

2. The EGS Collab project, Experiment 1

The EGS Collab project is an ongoing *in situ* experiment designed to investigate the stimulation of fractures in rock and the circulation of fluids in the stimulated fracture network at an intermediate scale (tens of meters, intermediate between lab and field scales) for EGS applications (Kneafsey et al., 2019; White et al., 2019). The project is planned to have three phases of experiments, and the Experiment 1 testbed is located in a predominately phyllite rock mass, approximately 1478 m below ground surface, on the western side of the West Access Drift on the 4850 level within the Sanford Underground Research Facility (SURF) in South Dakota, USA. In this section, we briefly describe the components of this experiment that are relevant to the present study.

2.1 Well configuration

Eight wells were drilled from the drift wall into the testbed, including an injection well, a production well and six monitoring wells (Fig. 1(a) and (b)). The injection well (E1-I) was drilled nominally in the direction of the minimum horizontal principal stress, so as to generate hydraulic fractures largely perpendicular to the wellbore according to geomechanics principles (Hubbert and Willis, 1957). Note that the local *in situ* stress orientation had been determined in an earlier experiment (Oldenburg, et al., 2017) and was verified by Experiment 1 results (Kneafsey et al., 2020). The production well (E1-P) was parallel to E1-I and approximately 10 m to the east of E1-I. Four monitoring wells (E1-PDT, E1-PDB, E1-PST and E1-PSB) were drilled parallel to the expected hydraulic fracture plane, and the other two monitoring wells (E1-OT and E1-OB) were largely orthogonal to the expected hydraulic fracture.

2.2 Geological and geophysical investigations

The temperature conditions in the testbed was investigated through several temperature surveys in 2009 and 2017 as well as a numerical simulation (Dobson and Salve, 2009; White et al., 2018). Apart from of the native geothermal gradient, the many decades of mining and research operations have created a largely radial temperature gradient around the West Access Drift into the testbed. Wellbore televiewer and acoustic logs were acquired, and cores were retrieved throughout the eight wells (approximately 467 m in total length) to map the natural fracture network in the testbed. Multiple geophysical techniques, including cross-hole seismic survey, continuous active-source seismic monitoring (CASSM), microseismic, electrical resistivity tomography (ERT) and distributed temperature sensing (DTS), were used to characterize the experiment site, and to monitor the evolution of the testbed, particularly the evolution of the fluid-conducting fracture. Sensors for these geophysical monitoring techniques were deployed in the six monitoring wells to obtain high-resolution measurements continuously before, during, and after fracture stimulation to obtain high-resolution measurements. A sewer camera was deployed in E1-P during one of the stimulations to directly observe fluid flow into the production well and identify possible intersection(s) of hydraulic fracture(s) with E1-P.

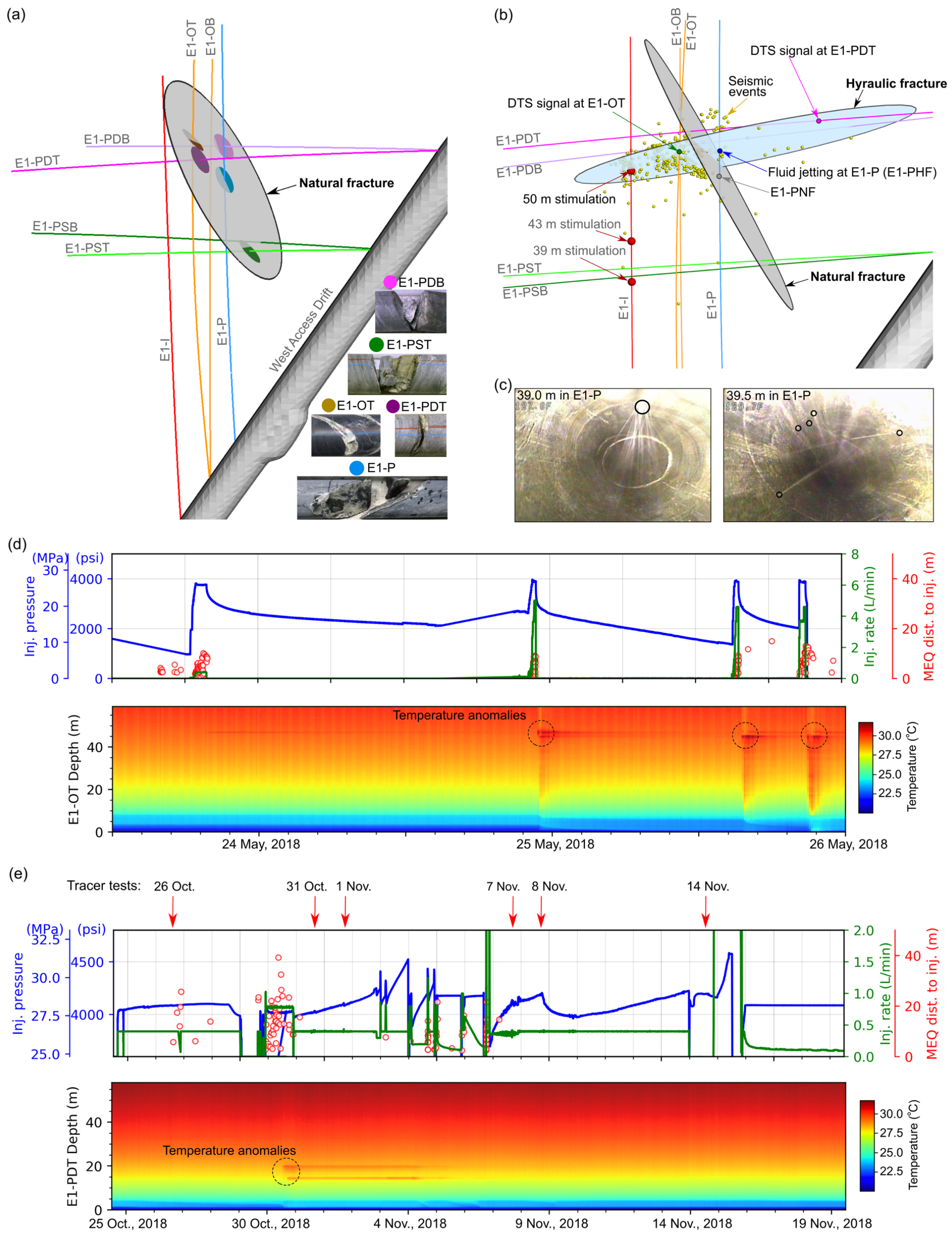

Fig. 1 The EGS Collab experiment testbed and key observations during hydraulic stimulation and water circulation. (a) Configuration of the eight wellbores. Five natural fracture traces identified from wellbore images of E1-P, E1-OT, E1-PDT, E1-PDB and E1-PST are shown as small disks. The images of core segments corresponding to the five fracture traces are also

shown. A fitted plane (gray ellipse) representing the natural fracture, named the "OT-P Connector" is constructed. (b) Spatial distribution of microseismic events from May to June and October to November, 2018. Locations of the observed fluid jetting in E1-P and DTS anomalies along E1-OT and E1-PDT are annotated. Based on these and other observations, a plane (light blue ellipse) representing the induced hydraulic fracture is constructed. (c) Fluid jetting observed in E1-P at 39.0 and 39.5 m on 25 May, 2018. The black circles annotate jetting points on the wellbore wall. (d) Injection parameters and temperature profile along E1-OT from 23 May to 25 May 2018. The red circles in the upper graph annotate the seismic events during the stimulation. The dashed black circles in the lower graph annotate the observed temperature anomaly along E1-OT. (e) Injection parameters and temperature profiles along E1-PDT during a water circulation test from 24 October to 20 November 2018.

2.3 Hydraulic stimulations and tracer tests

Multiple hydraulic stimulations have been performed at three depths in well E1-I, 39 m (128 ft), 43 m (142 ft) and 50 m (164 ft) in 2018. There was no indication of strong hydraulic interference between the fractures stimulated from these three depths. This work focuses on the fracture system stimulated at the 50 m interval in E1-I.

A water circulation test was conducted between 24 October and 20 November, 2018 by injecting into an interval between a set of straddle packers set at the 50 m depth of E1-I to characterize the stimulated fracture network. The time histories of injection rate, injection pressure and observed microseismic events are presented in a condensed form in Fig. 1(e). In general, an injection rate of 400 ml/min was used for the majority of the test window, with a few exceptions as shown in Fig. 1(e). According to the aforementioned temperature surveys and simulations, rock temperature at the 50 m interval in E1-I is approximately 30 °C, and the injection temperature during the water circulation test was mostly maintained at 30 °C, achieving a nearly isothermal condition. Note that the microseismic events, observed between 26 and 31 October and between 2 and 6 November, indicate that the stimulated fracture network may have changed during the circulation test. It was observed in the field that the stimulation activities between 3 November and 8 November caused the break of grouting/seal in E1-OT, leading to a significant increase in the outflow rate at E1-OT.

During the water circulation test, a series of tracer tests were conducted using different tracers, including conservative tracer (C-Dots and chlorine), reactive tracer (cesium, lithium, rhodamine-b, and fluorescein) as well as DNA tracer (Mattson et al., 2019a, 2019b; Zhang et al., 2019). C-Dots is a nanoparticle tracer consisting of a carbon core decorated with a highly fluorescent polymer (Hawkins et al., 2017b). For each test, tracers were first mixed with water and then injected into the fracture network through the 50 m depth interval. Serial water samples were collected for approximately 8 to 24 hours from the production and monitoring wells. The measurements and analysis of tracer concentrations in these water samples are detailed in Mattson et al. (2019a). In our stochastic modeling, we analyze the six C-Dots tracer tests as summarized in Table 1. Outflow rates at different wells during the six tracer tests are also shown in Table 1. Note that Table 1 only includes the volumetric flow rates from E1-P, E1-OT, E1-PDT, E1-PST and E1-PDB. Water also leaked into the mine drift from other locations, including wells not monitored for flow rates and natural fractures intersecting the drift. While fluid flowed out from five monitoring wells, C-Dots were only detected at E1-P and E1-OT (Fig. 2) within the measurement windows. Note that water and C-Dots flowed out of E1-P from two locations separated from each other using a straddle-packer assembly. One is the location at approximately 39.5 m deep, where fluid jetting was observed during the stimulation activities in May (Fig. 1(c)), and the other location is approximately 2.2 m shallower. We denote these two locations as E1-PHF and E1-PNF (HF=hydraulic fracture(s), NF=natural fracture(s), as will be explained in section 3.1) respectively (Fig. 1(b)). Corresponding to the changes of fracture flow field due to the aforementioned stimulation activities and the leakage of E1-OT, tracer breakthrough curves in Fig. 2 changed remarkably from 26 October to 31 October, and also from 1 November to 7 November.

Table 1 Six C-Dots tracer tests between 31 October and 14 November 2018. Outflow rates at different wells are also listed.

Date (in 2018)	Tracer inj. duration (min)	Tracer inj. concentration C_0 (ppm)	Outflow rate (mL/min)					
			E1-PHF	E1-PNF	E1-OT	E1-PDT	E1-PDB	E1-PST
26 Oct.	7.60	610	123.0	120.0	26.0	2.1	2.5	66.0
31 Oct.	5.00	305	82.0	75.0	9.0	78.0	5.9	40.0
1 Nov.	5.05	546	85.0	70.0	10.0	78.0	4.4	40.0
7 Nov.	5.12	623	40.0	35.0	118.0	10.0	2.5	15.0
8 Nov.	5.23	217	40.0	30.0	113.0	5.0	0.0	11.6
14 Nov.	5.08	160	54.0	26.0	190.0	4.0	1.0	11.0

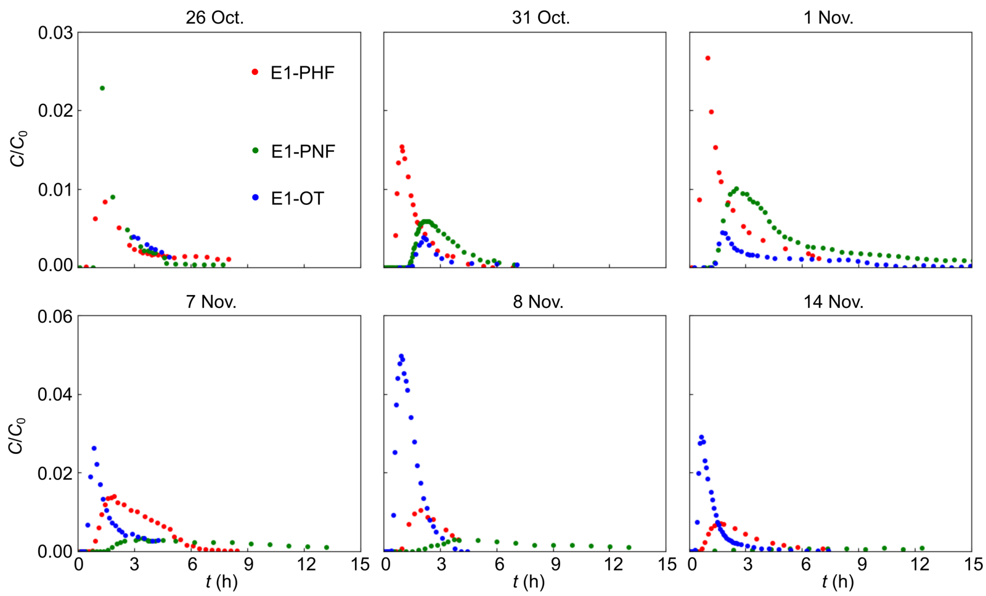

Fig. 2 Relative tracer concentration at E1-PHF, E1-PNF and E1-OT for the six C-Dots tracer tests.

3. Model and methodology

In this section, we first develop a fracture network model based on the comprehensive field observations and measurements, and then describe the methodology for forward modeling of fluid flow and tracer transport processes in the fracture network model, including the fracture coupling strategy, model parameterization, and numerical implementation. The last part further details the framework of the stochastic tracer modeling. Fig. 3 provides a summary of the model and methodology in the present study.

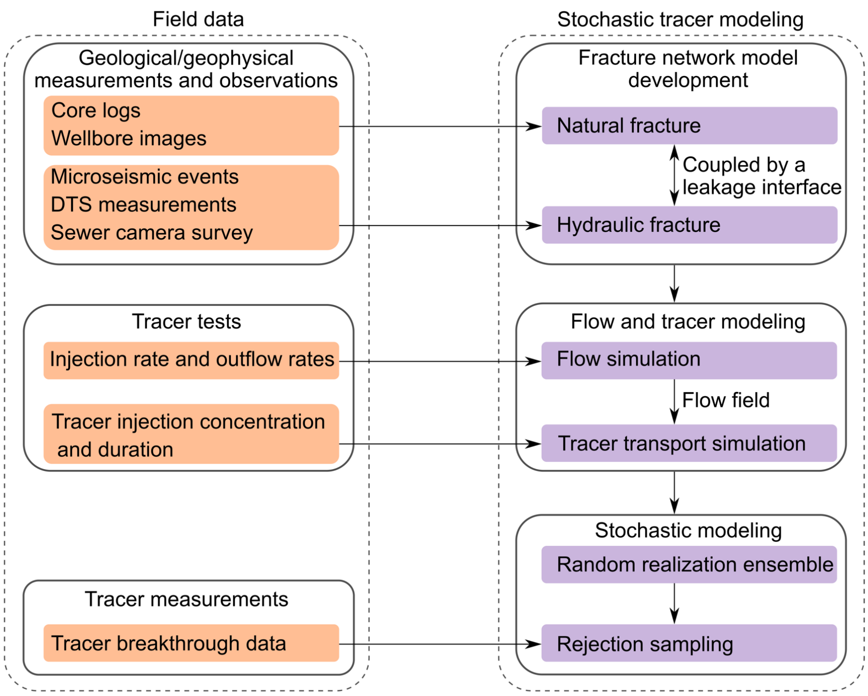

Fig. 3 Summary of the model and methodology in the present study.

3.1 Fracture network model

We first analyze the natural and hydraulic fractures relevant to the current study according to geological, geophysical and geochemical data, including core logs, wellbore images, microseismic events during hydraulic stimulations and the water circulation test, DTS measurements in the monitoring wells, microbial/geochemical data of reservoir indigenous fluids, and a sewer camera survey of E1-P.

Natural fractures. From core logs and wellbore images, 206 natural fracture traces were identified, and their properties and states are quite different: 130 of them are cemented fractures without apparent opening, 71 of them are partially open with limited aperture, and five of them are naturally flowing fractures with relatively large aperture. Considering the commonly recognized cubic relationship between aperture and fracture permeability, the flow and transport processes in the fracture network are dominated by the five naturally flow fractures, and most of the identified natural fractures actually do not or only slightly participate in the fluid flow and tracer transport processes. A major natural fracture connecting E1-OT and E1-P (also called OT-P connector) was inferred from three naturally flowing fracture traces and two partially open fracture traces (Fig. 1(a)). The five natural fracture traces were found in E1-P, E1-OT, E1-PDT, E1-PDB and E1-PST respectively, and they seem to conform to the same planar structure, not only in terms of locations but also in terms of local orientations (Fig. 1(a)). Additionally, a subset of the five wells had significant natural flows bearing microbial community signatures highly similar with each other, corroborating natural fracture connectivity (Zhang et al., 2019). Due to the much higher permeabilities of the five natural fracture traces compared with that of the other natural fracture traces, we believe the OT-P connector was the predominant natural fracture that participated in the flow and transport processes during the water circulation and tracer tests (Kneafsey et al., 2019).

Hydraulic fracture. Multiple hydraulic stimulations were performed on the E1-I 50 m interval between 22 May and 25 June, 2018. Each stimulation lasted up to 80 minutes and used injection rates up to 5.5 L/min. The stimulated hydraulic fracture can be delineated through DTS measurements, microseismic events and a sewer camera survey of E1-P on 25 May 2018. DTS-measured temperature anomalies in E1-OT (first observed on 24 May, 2018) and E1-PDT (first observed on 30 October, 2018), as well as fluid jetting in E1-P (observed on 25 May, 2018) conform to a plane that is roughly perpendicular to the *in situ* minimum principal stress orientation and also aligns with the microseismic cloud (Fig. 1(b)). Consequently, we believe this plane describes a stimulated hydraulic fracture.

A fracture network model involving a hydraulic fracture and a natural fracture (Fig. 4(a)) is then developed according to the above analysis. To account for the influence of other natural fractures, we included two “sinks” on the periphery of the developed fracture network model (as will be illustrated in section 3.2.2). Note that the two outflow locations in E1-P, denoted as E1-PHF and E1-PNF in section 2.3, are intersections between E1-P and the hydraulic fracture and the natural fracture respectively (Fig. 4(b)). We acknowledge that matrix diffusion is not represented due to the absence of matrix in the fracture network model. Nevertheless, considering the low matrix porosity (0.01), matrix permeability (5×10^{-18} m^2), and the short tracer injection durations (5 ~ 7.6 minutes) of the C-Dots tracer tests in Table 1, matrix diffusion is unlikely to have a significant effect on the tracer transport process (Becker and Shapiro, 2003; White et al., 2018; Zhou et al., 2018).

3.2 Modeling of fluid flow and tracer transport

3.2.1 Coupling of the hydraulic and natural fractures

We couple the hydraulic and natural fractures by treating a segment of the intersection line between the two fractures as the connection (i.e. a leakage interface) between them. Fluid carrying tracer flows from the hydraulic fracture to the natural fracture through this leakage interface. Instead of modeling the two fractures simultaneously, we model them separately in a sequential manner (Fig. 4(b)). The location, length, and leakage rate of this leakage interface are treated as parameters to be determined for the hydraulic fracture. The determined leakage parameters that fit the tracer breakthrough curves at E1-PHF and E1-OT, as well as the corresponding tracer concentration in the leaked fluid are then imposed as known boundary conditions for the natural fracture.

3.2.2 Parameter spaces for hydraulic and natural fractures

The uncertainties to be constrained in the stochastic modeling include fracture extents, the locations and sizes of sinks on the periphery of the two fractures, the aperture distributions of the two fractures, longitudinal and transverse dispersivities, as well as the location, length, and flow rate of the leakage interface between the two fractures. The parameterization of these uncertainties is explained below, with the ranges of corresponding parameters listed in Table 2.

- **Fracture extents**. There are no direct measurements to constrain the extents and shapes of the two fractures. The microseismic cloud (Fig. 1(b)) implies certain shape of the hydraulic fracture but events around the inferred perimeter of the fracture tend to be sparse and suffer from poor location certainty. Therefore, we mathematically represent each fracture using an ellipse within the determined fracture plane in Fig. 1. For the hydraulic fracture, the fracture center is estimated to be the center of the microseismic cloud, and the in-plane orientation of the ellipse is the overall propagation direction implied by the microseismic cloud. The extents of the hydraulic fracture are described by two parameters, i.e., the semi-axis lengths A_1 and A_2 as shown in Fig. 4(c). The ranges of A_1 and A_2 are characterized by microseismic events, DTS signals at E1-OT/E1-PDT and fluid jetting in E1-P. First, the hydraulic fracture extent should intersect with E1-I, E1-P and E1-OT (Fig. 1(b)) but also should not extend too far beyond the area indicated by seismic events. Second, because the hydraulic fracture was extended and intersected E1-PDT on 30 October (Fig. 1(b)), the value of the hydraulic fracture extent for tracer tests between 31 October and 14 November must be increased to account for this intersection. Therefore, the uncertainties of A_1 and A_2 for tracer tests between 31 October and 14 November are greater than those for the tracer test on 26 October (Table 2). The natural fracture's extent should at least cover the pentagon defined by the five intersections with wells in Fig. 1(a). Because the active flow area involving the HF-NF leakage interface and E1-PNF is at the center of the pentagon, the fracture area beyond the pentagon is expected to have little effect on the flow field. We fix the two semi-axis lengths of the natural fracture at 16.4 m and 15.2 m respectively.

- **Sinks**. Because injected fluid and tracer were not fully recovered in the six C-Dots tracer tests (Table 1), we assume a sink on the periphery of each fracture to account for fluid/tracer leakage to other natural fractures that are not explicitly described in the model (Fig. 4(c)).We use two parameters, angular orientation and length along the perimeter (θ and L for the hydraulic fracture, θ' and L' for the natural fracture), to describe the location and size of the sinks respectively (Fig. 4(c)).
- **Aperture distribution**. Fracture aperture has been widely studied in the literature (Moreno et al., 1988; Pyrak-Nolte and Morris, 2000; Tsang and Tsang, 1989). According to the measurements of core samples and observations of well logs, fracture aperture is generally spatially-autocorrelated and typically follows a gamma

distribution or a log-normal distribution (Bianchi and Snow, 1968; Gale, 1987). In the present study, we consider a relatively simple uniform aperture scenario as well as a spatially-autocorrelated heterogeneous aperture scenario. For the uniform aperture scenario, the aperture distribution is described by a single parameter (w and w' for the hydraulic and natural fractures, respectively), whereas for the heterogeneous aperture scenario, the aperture distribution is described by three parameters, including average aperture, standard deviation and correlation length ($\overline{w}$, σ and CL for the hydraulic fracture, $\overline{w}'$, σ' and CL$'$ for the natural fracture). We use the spherical variogram model to generate such a random heterogeneous aperture field following a log-normal distribution (Guo et al. (2016)). The ranges of parameters relevant to the aperture field are determined based on the following rationales. Wellbore images suggest that the aperture of the natural fracture (OT-P connector) may be up to several millimeters. A simple calculation using closed-form solutions for hydraulic fracture growth (Mack and Warpinski, 2000) finds that for the rock properties and injection rates during stimulations, the aperture of the hydraulic fracture would not exceed several hundred microns. For the numerical models used herein, the meaningful range of the correlation length is constrained by the extents of the fractures and the mesh resolution.

- **Dispersivity**. The transverse dispersivity α_T is generally smaller than the longitudinal dispersivity α_L, and some previous studies assume that $\alpha_T = 0.1\alpha_L$ (Hecht-Méndez et al., 2013; Hermans et al., 2018; Juliusson and Horne, 2013). In our stochastic modeling, we adopt the same assumption and therefore only include α_L in the parameter space. In addition, since molecular diffusion coefficient (D_m) is much smaller than dispersion coefficient for tracer transport in fractures, we assume a constant $D_m = 3 \times 10^{-9}$ m^2/s in the model. The range of α_L is assumed to be 0.001 ~ 4 m based on previous studies (Novakowski et al., 1985; Vogt et al., 2012).

- **Leakage interface**. In the stochastic modeling, the geometrical intersection between the two fractures is fixed with a length of 9 m. The leakage interface is a segment of the intersection and is parameterized by three numbers, two describing the location and length (P_L and L_L) of the leakage interface, and one for leakage rate (q_L) from the hydraulic fracture to the natural fracture. We denote the start and end points of the fracture intersection as S and S' (Fig. 4(c)), and P_L is the distance between the leakage interface center and S. The following rule applies to L_L to prevent the leakage interface from extending out of the geometrical intersection: if $(P_L - L_L/2) < 0$, $L_L = 2P_L$; if $(P_L + L_L/2) > 9$, $L_L = 18 - 2P_L$. Note that the leakage rate is uniformly distributed along the leakage interface. The range of the leakage rate depends on the measured outflow rates, in that the leakage rate should be larger than the total outflow rates from the natural fracture (sum of flow rates from E1-PNF, E1-PST and E1-PSB), and smaller than the difference between the injection rate and the total outflow rates from the hydraulic fracture (sum of flow rates from E1-OT, E1-PHF, E1-PDT and E1-PDB).

Table 2 Ranges of parameters for the hydraulic and natural fractures.

Parameters	Range
Hydraulic fracture	
Major axis length A_1 (m)	8.0 ~ 11.5 for 26 Oct. test, 14.5 ~ 17.5 for other tests
Minor axis length A_2 (m)	7.5 ~ 11.5 for 26 Oct. test, 8.5 ~ 13.5 for other tests
Uniform aperture w (mm)	0.01 ~ 1
Average aperture $\overline{w}$ (mm)	0.05 ~ 1
Standard deviation σ (mm)	0.05 ~ 1
Correlation length CL (m)	4 ~ 15

Longitudinal dispersivity α_L (m)	0.001 ~ 4					
Sink location θ (°)	0 ~ 360					
Sink length L (m)	3 ~ 15					
Leakage interface center P_L (m)	0.2 ~ 9.0					
Leakage interface length L_L (m)	0.2 ~ 9.0 (depends on P_L)					
Leakage rate q_L (ml/min)	26 Oct.	31 Oct.	1 Nov.	7 Nov.	8 Nov.	14 Nov.
	190 ~ 249	120 ~ 220	112 ~ 219	52 ~ 227	42 ~ 239	40 ~ 149
Natural fracture						
Uniform aperture w' (mm)	0.01 ~ 30					
Average aperture $\overline{w}'$ (mm)	0.1 ~ 10					
Standard deviation σ' (mm)	0.1 ~ 10					
Correlation length CL$'$ (m)	4 ~ 25					
Sink location θ' (°)	0 ~ 360					
Sink length L' (m)	3 ~ 20					

3.2.3 Fluid flow and tracer transport simulation

Fluid flow and tracer transport process in the hydraulic and natural fractures are simulated using a multi-physics simulation environment GEOS (Settgast et al., 2017), a massively-parallel multi-physics simulation platform developed at the Lawrence Livermore National Laboratory. GEOS provides a thermal-hydro-mechanical-chemical framework to simulate various physical processes occurring during reservoir stimulation and energy recovery. Applications include the simulation of immiscible fluid flow in fractures and rocks (Walsh and Carroll, 2013), heat recovery from geothermal reservoirs (Guo et al., 2016), geochemical transport and reaction (Walsh et al., 2013), hydraulic fracturing (Settgast et al., 2017), and so on. Guo et al. (2016) and Wu et al. (2019) described and verified the fluid flow and tracer transport modules in GEOS. In this study, fractures are represented by thin layers (4 mm and 20 cm thick in the mesh for the hydraulic and natural fractures, respectively) of porous media with the equivalent porosity $\phi = w/H$ and the equivalent permeability $k = w^3/12H$ according to the cubic law (Guo et al., 2016), where w is the aperture and H is the thickness of the fracture grid elements.

Both the hydraulic and natural fractures are discretized into hexahedral elements with an in-plane resolution of 0.2 m × 0.2 m. The finite volume method (FVM) is used to solve equations (1) and (2), and we use the upwind difference scheme to discretize equation (2) for tracer modeling. This scheme is known to cause numerical diffusion (Brasseur and Jacob, 2017; Leonard, 1979), but its effects on simulated tracer transport are observed to be negligible compared with the effects of advection and physical dispersion as simulated. The flow field is first solved from equation (1), and then used in equation (2) to solve for tracer concentration. For fluid flow simulation, the injection rate (400 mL/min) and the measured outflow rates listed in Table 1 are used as boundary conditions. For tracer transport simulations, the tracer injection parameters (injection concentration and duration) in Table 1 are also used as boundary conditions. Except for two sinks on the periphery of the two fractures, the boundaries along the perimeters of the hydraulic and natural fractures are assumed to be impermeable to both fluid and tracer. Note that the effect of temperature on fluid flow and tracer transport is not considered in the simulation due to the nearly isothermal injection condition and the temperature-insensitive nature of C-Dots.

3.3 Stochastic tracer modeling framework

For each tracer test, we first generate an ensemble of parameter sets using the Latin-hypercube sampling approach with each individual parameter following a uniform distribution (A_1, A_2, CL, CL$'$, θ, θ', L, L', P_L, L_L and q_L) or a log-uniform distribution (w, w', $\bar{w}$, $\bar{w}'$, σ, σ' and α_L) in its corresponding range in Table 2. Each parameter set corresponds to a stochastic realization of the flow system, for which the following workflow applies. 1) Based on the aperture parameters, a uniform or a spatially-autocorrelated heterogeneous aperture field is generated and applied to the fracture. 2) The steady-state flow field in the fracture is calculated based on the aperture field and boundary conditions mentioned in section 3.2.3. 3), The tracer transport process in the fracture is simulated with the flow field at steady state. The resultant residence time distribution is subsequently evaluated against measured tracer BTCs. GEOS itself is a massively parallelized code but in the current study, parallelization is only employed to simulate the many stochastic realization, with each realization simulated using one CPU core. Step (2) in the workflow costs a few seconds on a single core of Xeon E5-2695 v4. Step (3) needs to resolve the transient tracer transport process and costs between 14 seconds and 3.5 hours depending on the flow characteristics for the realization. A fracture flow model involving 50,000 realizations costs more than 40,000 core-hours, necessitating HPC power for a comprehensive study involving many models.

We then use a rejection sampling method to analyze the stochastic tracer modeling results in terms of the 90% confidence intervals of the simulated tracer breakthrough curves and the uncertainty quantification of model parameters. The procedure of the rejection sampling is described in Sun and Durlofsky (2017). The main steps are: (1) Generate a random variable p from a uniform distribution within the range [0, 1]. (2) Accept $\mathbf{m}$ as a posterior realization if $p \leq L(\mathbf{m})/S_L$, where $\mathbf{m}$ is a parameter set, $L(\mathbf{m})$ is the likelihood function and S_L is the maximum of the likelihood function. The likelihood function $L(\mathbf{m})$ is defined as

$$L(\mathbf{m}) = c \cdot \exp(-\tfrac{1}{2}R(\mathbf{m})) \quad (1)$$

where c is a normalization constant. $R(\mathbf{m})$ is a function evaluating the fitness between the simulated and measured tracer breakthrough curves. Sun and Durlofsky (2017) used the sum of the square error as $R(\mathbf{m})$ in their analysis. However, in the present study, we found the following function captures the most essential characteristics of the tracer BTCs and therefore is used as $R(\mathbf{m})$ in our analysis

$$R = \frac{1}{\sigma_\mathrm{e}^2}\left[\left(\frac{C_P^{sim.}}{C_P^{mea.}} - 1\right)^2 + \left(\frac{t^{sim.}}{t^{mea.}} - 1\right)^2 + \left(\frac{t_\mathrm{l}^{sim.}}{t_\mathrm{l}^{mea.}} - 1\right)^2 + \left(\frac{t_\mathrm{r}^{sim.}}{t_\mathrm{r}^{mea.}} - 1\right)^2\right] \quad (2)$$

where σ_e is the standard deviation of measurement errors. Note that we assume the measurement errors to be independent, identically distributed Gaussian random variables. For subsequent analysis, σ_e is assumed to be 0.3. The two superscripts "sim." and "mea." denote the results from simulation and measurement respectively. C_P and t are the magnitude of the peak concentration and the corresponding arrival time; t_l and t_r are the two times, before (left of) and after (right of) the peak, respectively, of the half-peak magnitude. This equation compares four parameters controlling the shape of a tracer breakthrough curve. To find peaks from a simulated tracer BTC, we adopt the *find_peak* function of the SciPy signal processing toolbox in Python (scipy.signal.find_peak), which can screen out non-prominent peaks (Jones et al., 2001). As shown in Fig. 2, each measured tracer BTC has only one peak. However, a simulated tracer BTC may have multiple peaks. We directly extend the misfit calculation method to a simulated BTC with multiple peak concentrations by applying equation (4) to every peak on the simulated tracer BTC, and then summing the calculated misfit values together. This leads to high misfit values for those realizations, naturally penalizing the realizations with multiple concentration peaks. Also note that for the hydraulic fracture, both the tracer BTCs at E1-PHF and E1-OT need to be quantified, and we sum the misfits for E1-PHF and E1-OT together as the total misfit. For the natural fracture, we only calculate the misfit for the tracer BTC at E1-PNF.

We first perform stochastic modeling for the hydraulic fracture according to the aforementioned workflow. The realization that yields the smallest total misfit is selected to attain the time-concentration curves along the leakage interface, with which we then perform the stochastic modeling for the natural fracture using the same workflow.

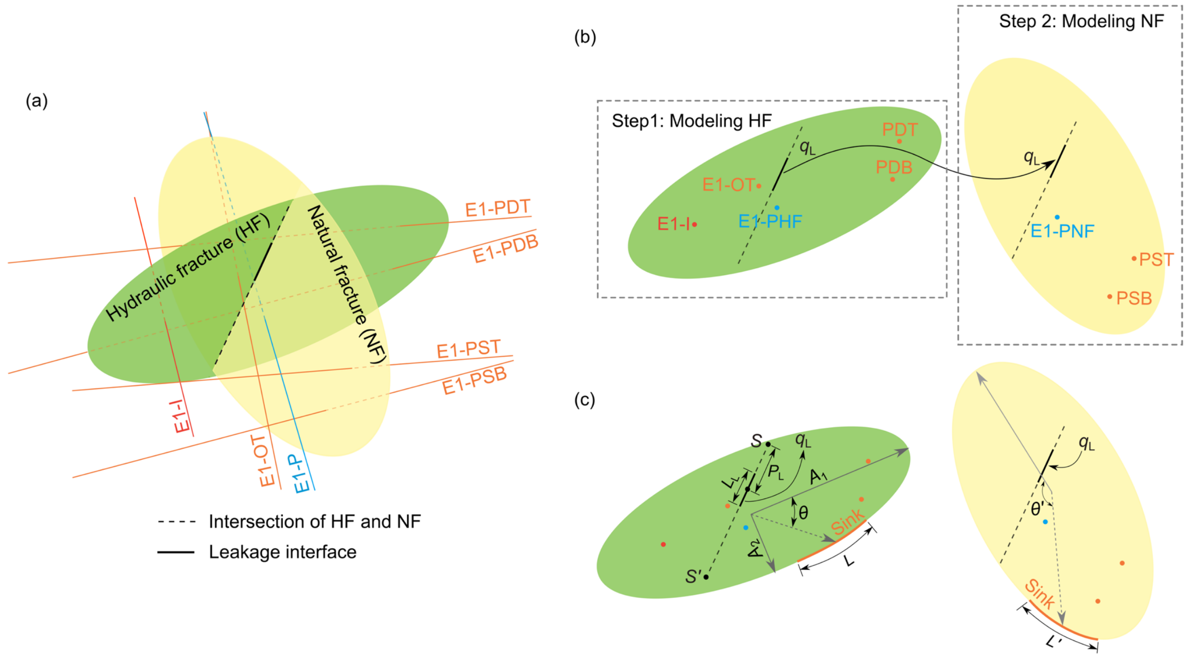

Fig. 4 The developed fracture network model and the modeling of tracer transport processes in the model. (a) Diagram of the fracture network model. The hydraulic (green) and natural fractures (yellow) are coupled by a conductive segment on their intersection. (b) Sequential modeling of tracer transport processes in the fracture network model. (c) Parameterization of the hydraulic and natural fractures. θ and θ' denotes the angles between the major semi-axis and the sink center for the hydraulic and natural fractures respectively.

4. Results of the stochastic modeling for the hydraulic fracture

4.1 Relationship between the total misfit and individual parameters

We start the analysis with the relatively simple uniform aperture scenario with nine parameters for the hydraulic fracture. Approximately 50,000 realizations were performed for each tracer test and the scatter plots between individual parameters and the total misfit are shown in Fig. 5. Note that only the scatter plots for w, θ, α_L and P_L are shown in Fig. 5, and those for the other parameters can be found in Fig. S1 in Supplementary Material. The total misfit R varies in a wide range and Fig. 5 only shows the realizations with a total misfit smaller than 10^4. According to equation (4), if the differences of the four variables (C_P, t, t_l and t_r) between simulation and measurement all equal 15%, then the calculated misfit is 0.09, and the base 10 logarithm of the total misfit for the two tracer BTCs (E1-PHF and E1-OT) is -0.74. As shown in Fig. 5, most of the performed realizations show a total misfit much larger than -0.74 and fail to reasonably match the measured tracer BTCs at E1-PHF and E1-OT simultaneously.

The nine parameters show different effects on the total misfit. We observe a strong dependence of the total misfit on aperture (w), sink location (θ), longitudinal dispersivity (α_L), and leakage interface location (P_L). For these parameters, we are able to identify concentrated value ranges (as shown by the 90% confidence intervals in the scatter plots in Fig. 5) according to the accepted parameter sets from the rejection sampling procedure, while for the other parameters, such a concentrated value range cannot be obtained. From the satisfactory realizations accepted by the rejection sampling procedure, we calculate the 90% confidence intervals for tracer breakthrough curves at E1-PHF and E1-OT (shadings in Fig. 5) to compare with the field tracer measurements (red and blue dots in Fig. 5). The results of the realization with the smallest total misfit (solid lines in Fig. 5) are also shown. The comparison indicates that the measured tracer breakthrough curves at E1-PHF and E1-OT are successfully reproduced simultaneously. We use the parameter values from the realization with the smallest total misfit as the best estimates for these parameters (Table 3).

(a): Results of the tracer test on 26 Oct.

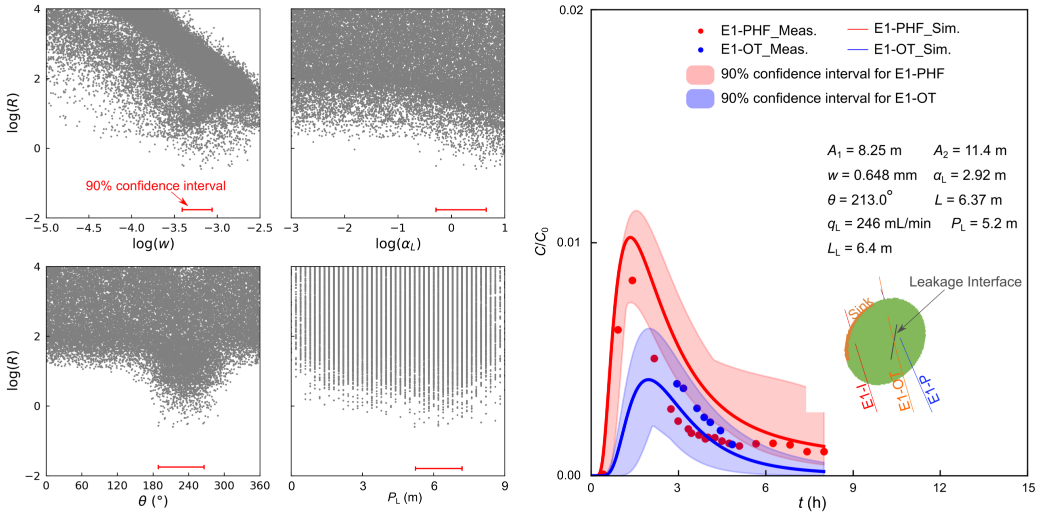

(b): Results of the tracer test on 31 Oct.

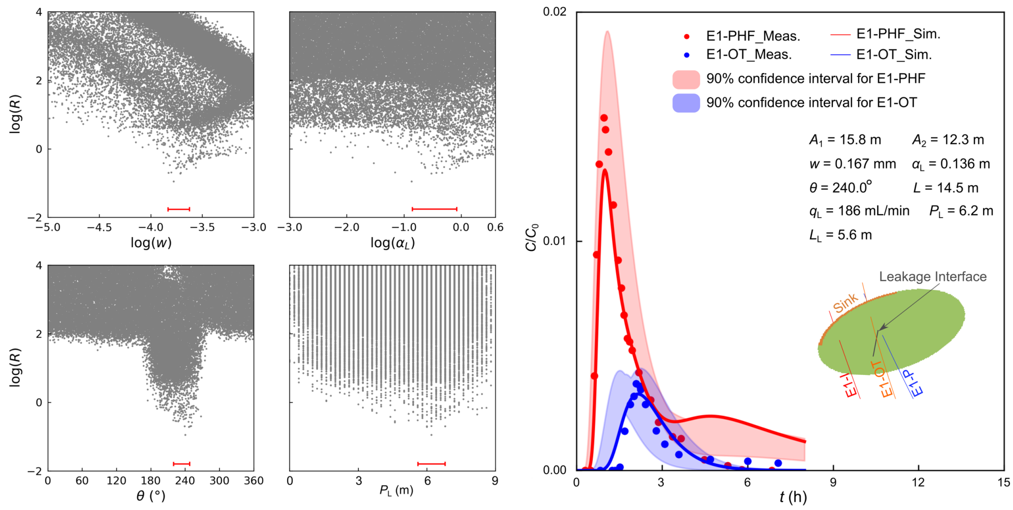

(c): Results of the tracer test on 1 Nov.

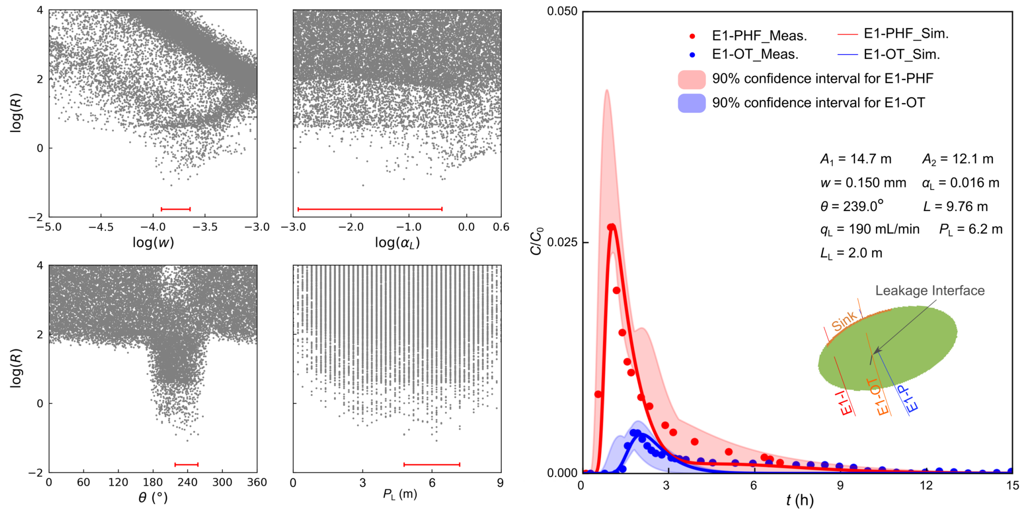

(d): Results of the tracer test on 7 Nov.

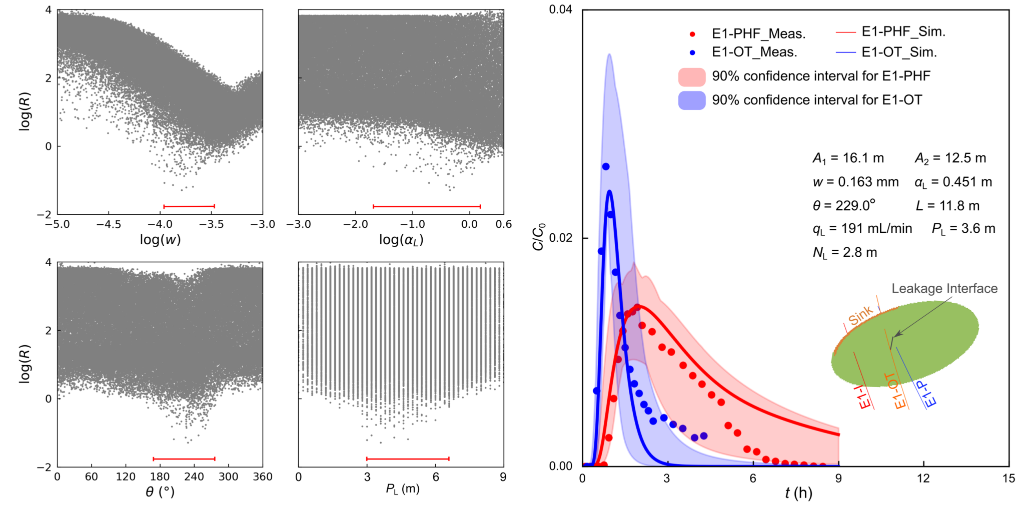

(e): Results of the tracer test on 8 Nov.

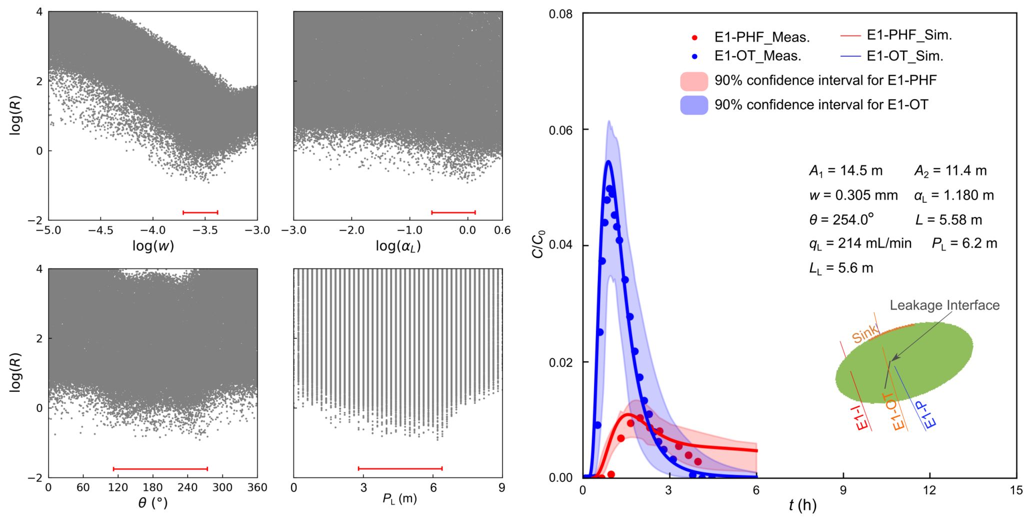

(f): Results of the tracer test on 14 Nov.

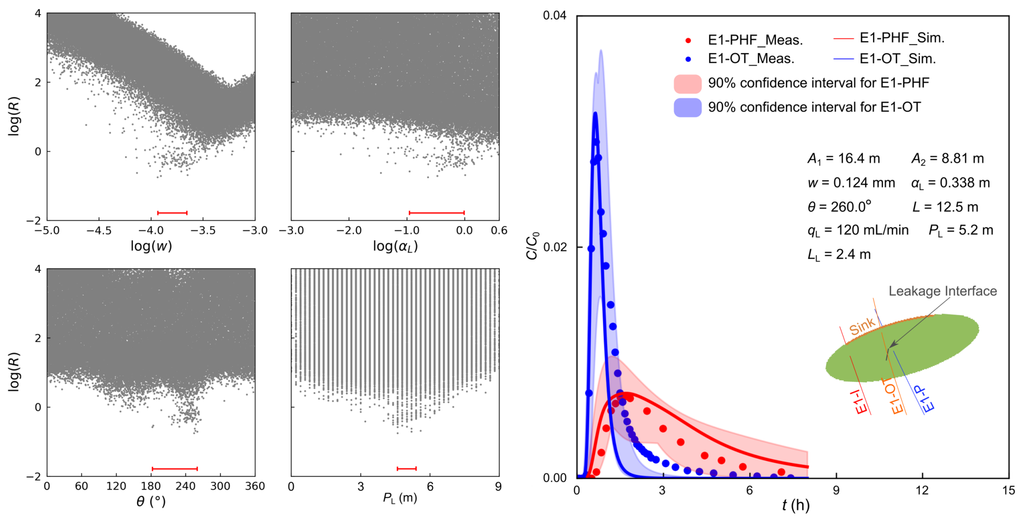

Fig. 5 Stochastic modeling of tracer transport in the hydraulic fracture under the uniform aperture scenario. (a) ~ (f) show the results for tracer tests on 26 and 31 October, 1, 7, 8 and 14 November respectively. In each subfigure, the scatter plots in the first two columns show the variation of the total misfit as a function of aperture (w), sink location (θ), longitudinal dispersivity (α_L), and leakage interface location (P_L), respectively. Each point represents a realization. The red line segments in these scatter plots denote the 90 % confidence interval of parameters. The figure to the right compares the measured and simulated tracer breakthrough curves at E1-PHF and E1-OT. The red and blue shadings are the 90% confidence intervals for tracer breakthrough curves at E1-PHF and E1-OT respectively. Results of the realizations with the smallest total misfit are also shown, including the simulated tracer breakthrough curves (solid lines), parameter values, as well as the locations of the sink and leakage interface.

4.2 Sensitivities of individual parameters

The Sobol′ total sensitivity index is a measurement of the contribution of each parameter to the variance of the total misfit (Sobol′, 1993), and can be used to identify critical parameters that dominate the tracer transport process. As shown in Fig. 6, the Sobol′ total sensitivity indices show similar patterns for the six tracer tests. The tracer transport process in the hydraulic fracture is dominated by the aperture (w) and sink location (θ), while fracture extents (described by A_1 and A_2), leakage rate (q_L) and the length of the leakage interface (described by L_L) actually show little effects, especially for the tracer tests on 26 October, 1, 7, 8 and 14 November. As a result, the uncertainties in w and θ are appropriately constrained from the stochastic tracer modeling, while the uncertainties in A_1, A_2, q_L, and L_L cannot be further constrained. The result of Sobol′ sensitivity analysis is consistent with the scatter plots in Fig. 5 in that the more sensitive the parameter, the easier it is to identify an optimal value for the parameter.

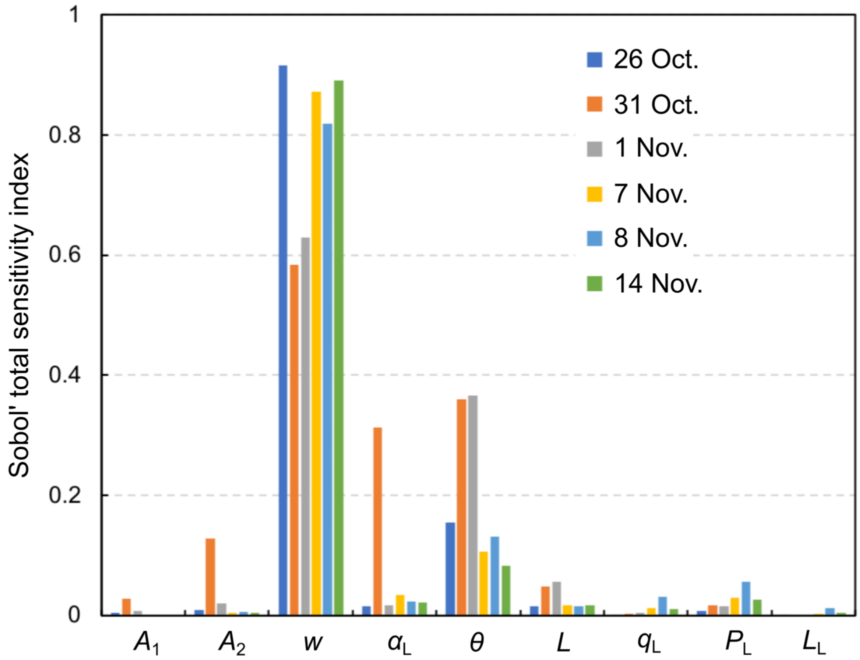

Fig. 6 Sobol′ total sensitivity indices of the nine parameters pertaining to the hydraulic fracture under the uniform aperture scenario.

Table 3 Estimates of aperture (w), sink location (θ), longitudinal dispersivity (α_L), and leakage interface location (P_L) for the hydraulic fracture under the uniform aperture scenario.

Date of tracer test (2018)	Estimates of parameters			
	Aperture w (mm)	Longitudinal dispersivity α_L (m)	Sink location θ (°)	Leakage interface center location P_L (m)
26 October	0.648	2.92	246	5.2
31 October	0.167	0.14	240	6.2
1 November	0.150	0.02	239	6.2
7 November	0.163	0.45	229	3.6
8 November	0.305	1.18	254	6.2
14 November	0.124	0.34	260	5.2

4.3 Heterogeneous aperture scenario

Previous experimental observations and theoretical studies indicate that flow channeling is a common phenomenon in fracture networks (Becker & Shapiro, 2000; Fu et al., 2016; Guo et al., 2016; Moreno et al., 1988; Hawkins et al., 2017b). Although the uniform aperture scenario is able to match the measured tracer breakthrough curves at E1-PHF and E1-OT simultaneously, it could be illuminating to further model the tracer tests under the heterogeneous aperture scenario where flow channeling is generally much stronger than that in the uniform aperture scenario. Here we take the tracer test on 31 October as an example, for which 400,000 realizations were modeled (Fig. 7). Similarly, we only show the scatter plots for aperture parameters ($\overline{w}$, σ and CL), longitudinal dispersivity (α_L), sink location (θ) and leakage interface location (P_L) in Fig. 7(a), and scatter plots for other parameters are provided in Fig. S2 in Supplementary Material. Compared with the uniform aperture scenario, the heterogeneous aperture scenario involves more parameters, and a larger number of satisfactory realizations obtained from the rejection sampling procedure can match the tracer breakthrough curves at E1-PHF and E1-OT simultaneously (as shown in Fig. 7(b)). However, the heterogeneous aperture fields for these satisfactory realizations are quite different from each other (Fig. 7(c)). Although the Sobol′ total sensitivity analysis shows that the average aperture ($\overline{w}$) and sink location (θ) are dominant parameters under the heterogeneous aperture scenario (Fig. 8), the values of the aperture parameters ($\overline{w}$, σ and CL) cannot be constrained as under the uniform aperture scenario. However, a concentrated value range for θ can still be identified from the obtained satisfactory realizations, which is consistent with the results under the uniform aperture scenario (Table 3). The stochastic model seems to be overfitted under the heterogeneous aperture scenario for the available tracer measurements.

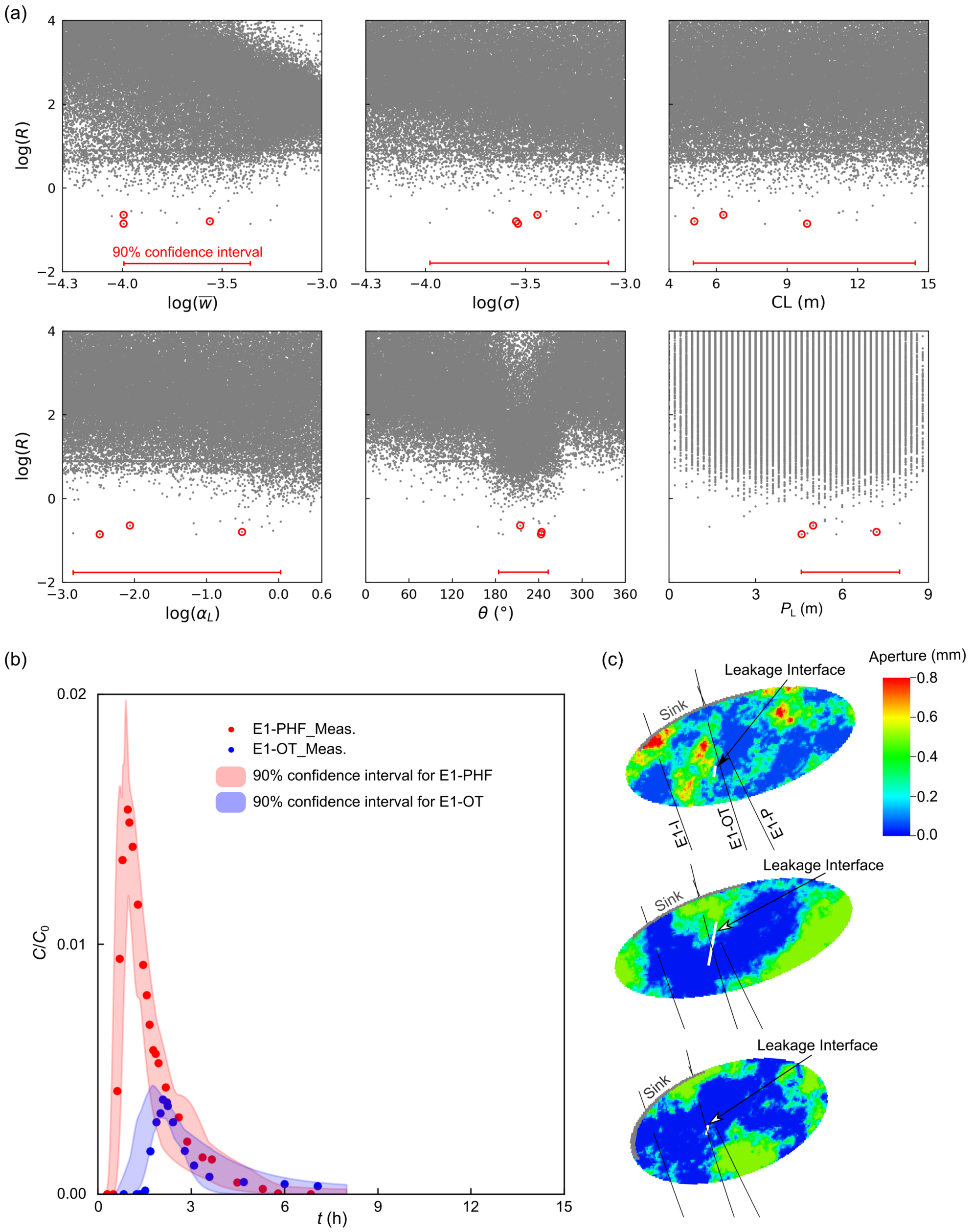

Fig. 7 Stochastic modeling of tracer transport in the hydraulic fracture under the heterogeneous aperture scenario for the tracer test on 31 October. (a) Scatter plots of the total misfit as a function of individual parameters. The red line segments annotate the 90% confidence interval of parameters. (b) Comparison of the tracer BTCs at E1-PHF and E1-OT from measurement and satisfactory realizations. The red and blue shadings are the 90% confidence intervals for tracer breakthrough curves at E1-PHF and E1-OT respectively. (c)

Aperture distribution, location of the sink and leakage interface for three satisfactory realizations. The three realizations are also annotated by red circles in (a).

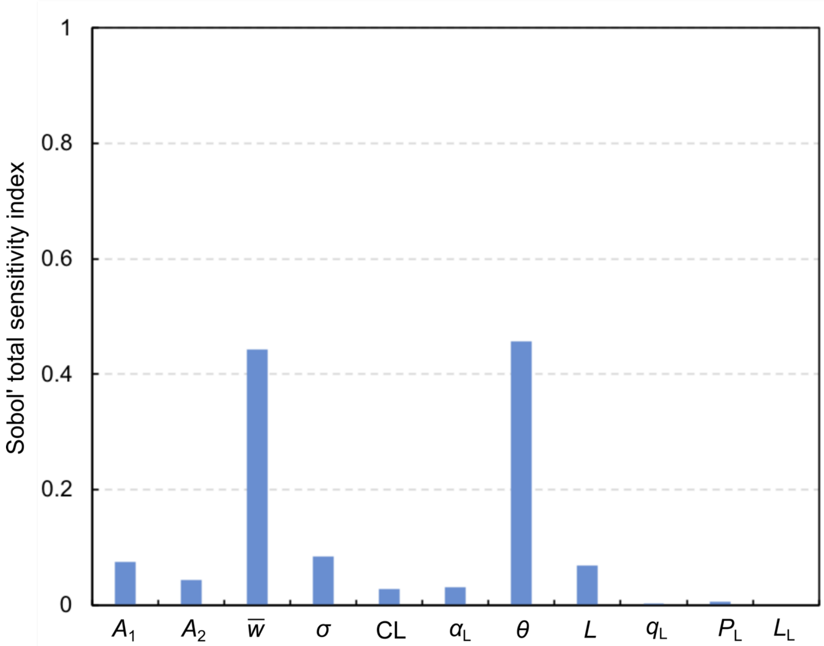

Fig. 8 Sobol′ total sensitivity indices of the 11 parameters pertaining to the hydraulic fracture for the modeling of the tracer test on 31 October under the heterogeneous aperture scenario.

5. Results of the stochastic modeling for the natural fracture

For each tracer test, we select the realization with the smallest total misfit under the uniform aperture scenario (parameters listed in Fig. 5) to attain the necessary "upper-stream" information to perform stochastic modeling of flow and transport processes in the natural fracture. The information includes the leakage rate q_L, leakage interface location and length (P_L and L_L), as well as the time-concentration curves for each leakage element.

5.1 Uniform aperture scenario

Similar to the modeling of the hydraulic fracture, we start the analysis of the natural fracture with the uniform aperture scenario. Since only three parameters are involved (w', θ' and L'), we performed around 15,000 realizations for each tracer test. The scatter plots of the total misfit as a function of the three parameters are shown in Fig. S3 in Supplementary Material. Fig. 9 compares the tracer breakthrough curve at E1-PNF from measurement and the realization with the smallest total misfit. Although the misfit results clearly favor a specific range for w', the tracer breakthrough curves at E1-PNF cannot be matched to a reasonable level. The modeling results for 26 October tracer test in Fig. 9 indicate an average aperture of 0.1 mm, while the core logs retrieved from E1-P indicate that the aperture in the natural fracture is several millimeters. Therefore, the uniform aperture scenario is unlikely to correctly simulate the tracer transport process in the natural fracture.

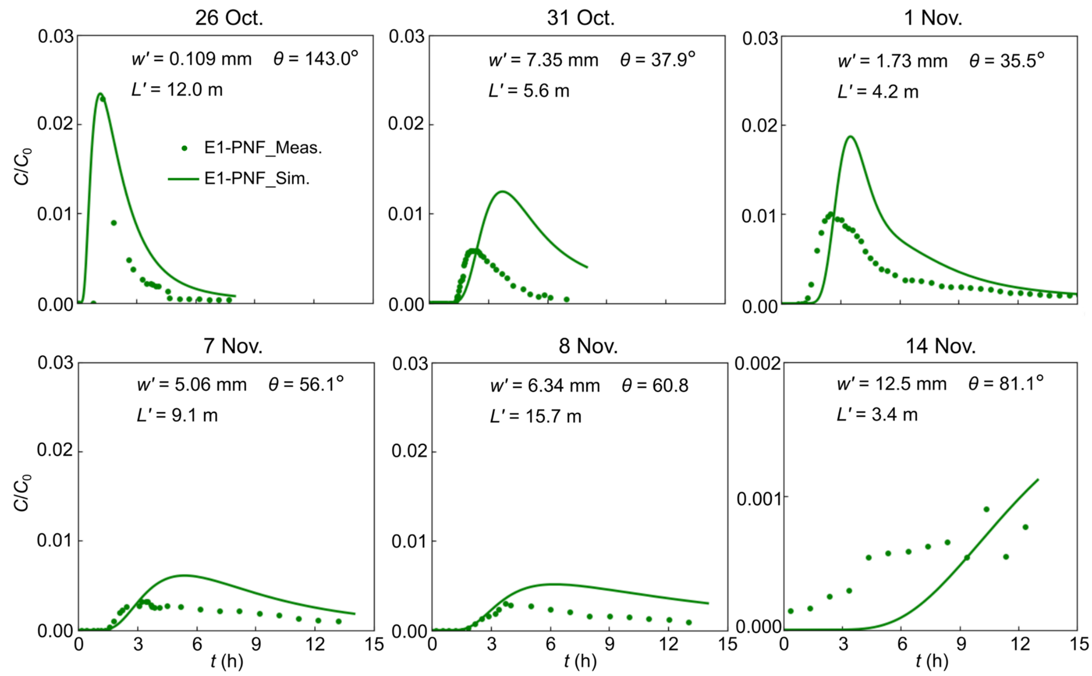

Fig. 9 Fitness of the tracer breakthrough curve at E1-PNF under the uniform aperture scenario for the six tracer tests.

5.2 Heterogeneous aperture scenario

We then assume a spatially-autocorrelated heterogeneous aperture distribution in the natural fracture. Around 50,000 realizations were performed for each tracer test (Fig. 10). Many satisfactory realizations that match the tracer breakthrough curve at E1-PNF almost equally well are obtained from the rejection sampling procedure, and the corresponding parameters in these satisfactory realizations span relatively large ranges in the parameter space as shown by the red circles in the scatter plots in Fig. 10 (scatter plots for other parameters are provided in Fig. S4 in Supplementary Material). We also show the aperture distribution in the natural fracture from one of the satisfactory realizations, and more results can be found in Fig. S5 in Supplementary Material. For tracer tests between 26 October and 8 November, the 90% confidence interval of the tracer breakthrough curve at E1-PNF agree well with the measured tracer data. However, for the tracer test on 14 November, due to the lack of tracer concentration measurements beyond 12 hours (due to field operational constraints), the fitting of the tracer breakthrough curve is difficult and the corresponding 90% confidence interval indicates a large uncertainty.

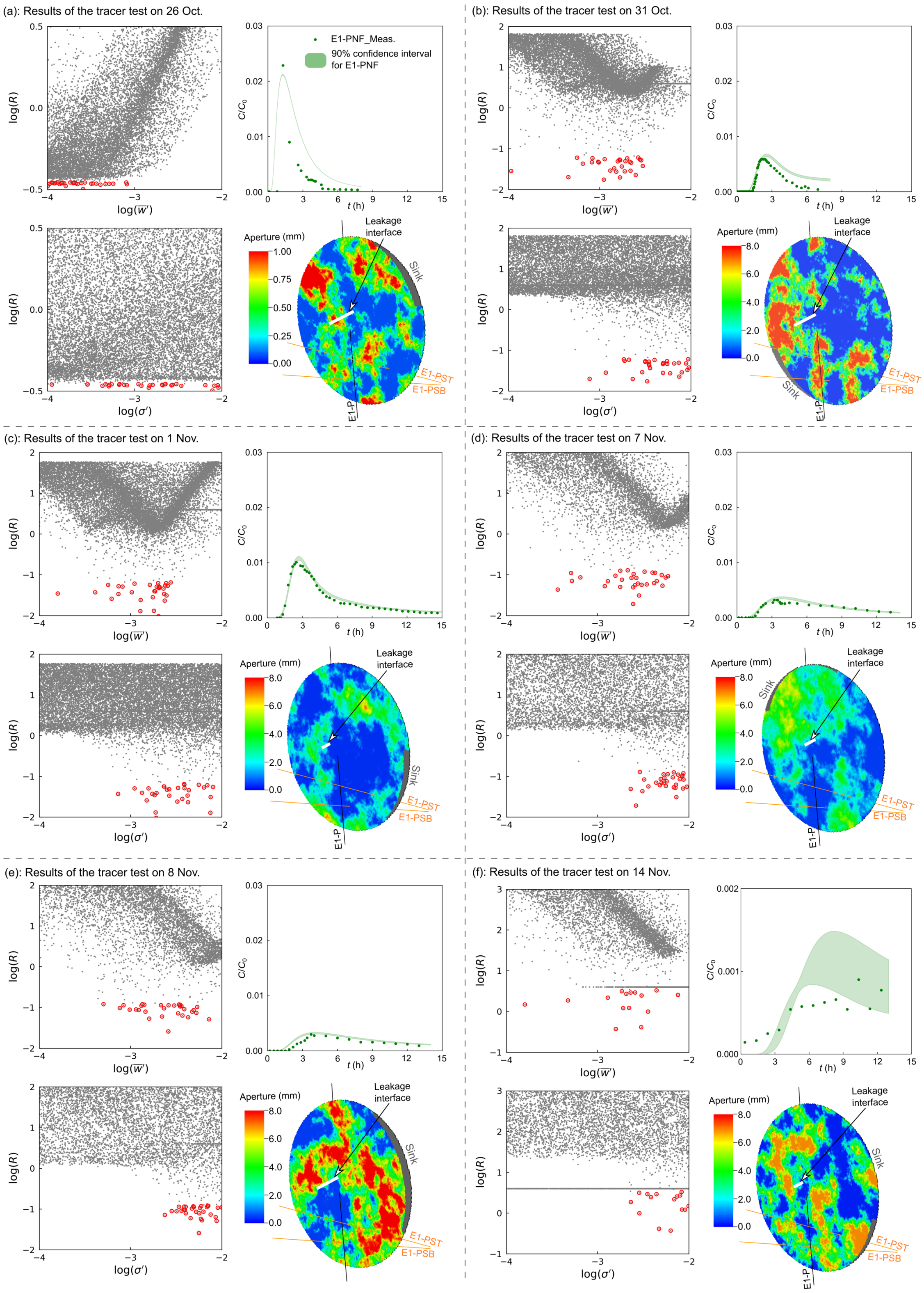

Fig. 10 Stochastic modeling of tracer transport in the natural fracture under the heterogeneous aperture scenario. (a) ~ (f) show the results for tracer tests on 26 and 31 October, 1, 7, 8 and 14 November respectively. In each subfigure, we show the scatter plot of the total misfit as

well as results from the obtained satisfactory realization. The red circles in the scatter plots annotate satisfactory realizations. The green shadings are the 90% confidence intervals for the tracer breakthrough curve at E1-PNF. The aperture distribution from one of the satisfactory realizations is also shown.

6. Discussions

6.1 Consistency of stochastic modeling results with other field observations

The following field observations were not used to constrain the stochastic models. However, the agreement between the modeling results and these observations serves as additional validation of the modeling work.

Aperture of the natural fracture. Although the aperture of the natural fracture cannot be constrained from the stochastic modeling results, a rough estimate of its value can be obtained from the aperture distributions in Fig. 10. According to the satisfactory realizations for tracer tests between 31 October and 14 November, the average aperture is approximately 1 ~ 3 millimeters, which is in agreement with the value (several millimeters) estimated from core segments corresponding to the five fracture intersections in Fig. 1(a). The fact that no uniform aperture distribution in the natural fracture could fit the tracer data indicates that flow in the natural fracture is highly heterogeneous. This is consistent with the observation from the five core segments in Fig. 1(a), which show very different forms in terms of kinematic aperture and the mineral fillings.

Location of the sink on the hydraulic fracture. An interesting finding from the stochastic modeling is that fluid and tracer leaked out of the hydraulic fracture from its west boundary, meaning that another natural fracture that is not explicitly included in our fracture network model was likely to intersect the west boundary of the hydraulic fracture. The existence of this natural fracture was confirmed in a later stimulation activity at the 43 m interval in E1-I on 20 December 2018, during which seismic events showed an apparent tendency to propagate northward and intersected the west boundary of the hydraulic fracture stimulated at the 50 m interval.

6.2 Inferring the evolution of fracture flow characteristics during the circulation tests

Direct observations of the measured outflow rates (Table 1) and tracer breakthrough curves (Fig. 2) indicate that the fracture flow field changed several times during the water circulation test from 24 October to 20 November, 2018. Two major changes can be identified: one taking place between tracer tests on 26 and 31 October and the other one between tracer tests on 1 and 7 November. By assuming that fracture flow models that reasonably fit the tracer data can represent the actual states of the fracture flow system, we could infer the nature of these changes from the stochastic modeling results.

Related to the first major change, the fitted aperture for the tracer test on 26 October is significantly larger than that for the five subsequent tests according to the results in Table 3. Both microseismic and DTS temperature measurements indicated significant eastward hydraulic fracture propagation during the 800 ml/min rate injection from 29 to 30 October. This seems to indicate that prior to this propagation, the hydraulic fracture was dilated to a larger aperture to accommodate the 400 ml/min circulation rate before 29 October. The hydraulic fracture propagation between 29 and 30 October enabled stronger hydraulic connection between the hydraulic fracture and the natural fracture system, thereby accommodating the injection rate without requiring much dilation of the fracture.

The second major change was likely caused by the redistribution of outflows among production and monitoring wells resulting from stimulation-induced damage to E1-OT sealing. The aperture of the hydraulic fracture remained almost constant between 1 and 7 November (Table 3). Before the damage to E1-OT, fluid and tracer had a strong tendency to flow in the direction from E1-I to E1-PHF due to the presence of the leaky interface and high outflow rate at E1-PHF. Therefore, tracer breakthrough was earlier and peak magnitude was larger at E1-PHF than that at E1-OT on 1 November. However, after E1-OT was damaged by stimulation on 6 November, outflow rate increased significantly at E1-OT and decreased at E1-PHF and E1-PNF, and fluid (and tracer) became easier to flow in the direction from E1-I to E1-OT. As a result, tracer breakthrough was earlier and peak magnitude was larger at E1-OT than that at E1-PHF on 7 November.

Although the heterogeneous aperture scenario for the natural fracture tends to over-fit the tracer data and the fitting results are nonunique, we could still gain critical insights into the changes in the natural fracture's flow field from the commonalities among the satisfactory fitting results. The satisfactory realizations statistically suggest that the average aperture ($\overline{w}'$) increased from 26 October to 14 November, as shown in Fig. 11. A particularly remarkable increase took place between 26 October and 31 October, likely a result of the hydraulic fracture propagation between 29 and 30 October. We could not point to a specific explanation for the increased aperture; it could be caused by an expansion of the active flow area on the fracture, thereby engaging more flow channels with larger apertures, or some geochemical causes, the discussion of which is beyond the scope of this work.

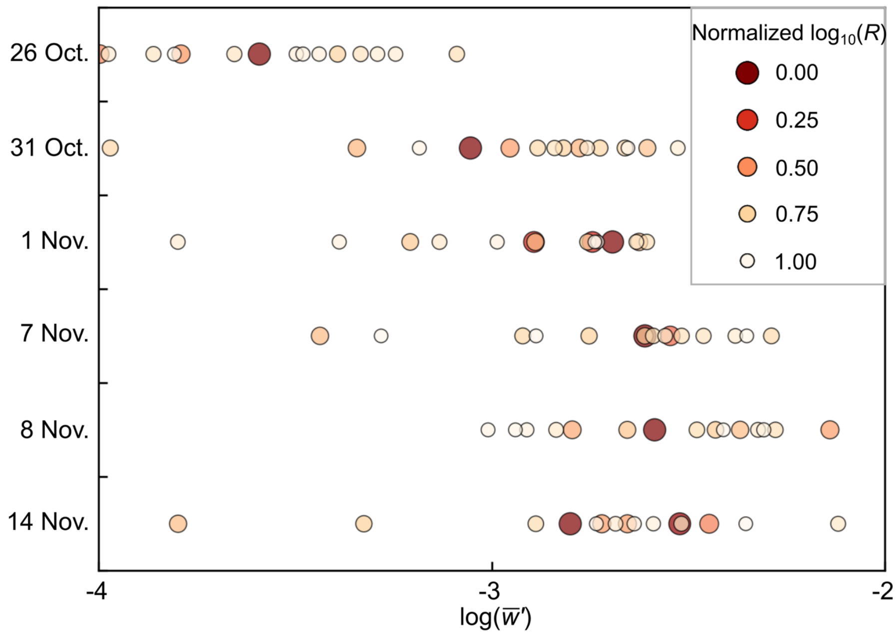

Fig. 11 Average aperture of the natural fracture from 15 satisfactory heterogeneous aperture realizations for each of the tracer tests on 26 and 31 October, 1, 7, 8 and 14 November. Each circle represents a satisfactory realization. We use both color and size to indicate the total misfit for the corresponding realization.

6.3 Effect of tracer data quality and quantity on stochastic modeling

Stochastic tracer modeling is inherently an inversion process to infer 3D flow and transport characteristics from time-series tracer data. The quality and quantity of available tracer data are essential for this inversion process. Based on the results of this study, we analyze the effect of tracer data quality and quantity on stochastic modeling.

First, any incompleteness in tracer breakthrough curves causes ambiguity in the interpretation of stochastic modeling results. As shown in Fig. 5(a), due to the lack of the ascending segment of the tracer breakthrough curve at E1-OT, the peak arrival time and peak magnitude cannot be used to accurately evaluate the fitness between the measured and simulated tracer breakthrough curve, which undoubtedly caused ambiguity in the selection of satisfactory realizations. On the other hand, as shown in Fig. 10(f), the breakthrough curve at E1-PNF does not have tail data beyond 12 hours. As a result, the stochastic modeling results show a large uncertainty in the simulated tracer breakthrough curve.

Second, sampling tracer concentrations at multiple locations in the flow network is crucial for resolving the spatial distribution of flow in the fractures. In this study, there are two tracer breakthrough curves (E1-PHF and E1-OT) available for the hydraulic fracture, and a satisfactory realization needs to match the two breakthrough curves simultaneously. If the misfit function had only accounted for one breakthrough curve, then the stochastic modeling results could no longer constrain model parameters. Take the tracer test on 31 October as an example. Had only one tracer breakthrough curve been matched (either at E1-PHF or E1-OT), we would have obtained more than 30 satisfactory realizations. Fig. 12 shows the results from four of these realizations. Among these satisfactory realizations, the values of the four critical parameters (w, θ, α_L and P_L) vary in large ranges and cannot be constrained such as in Fig. 5.

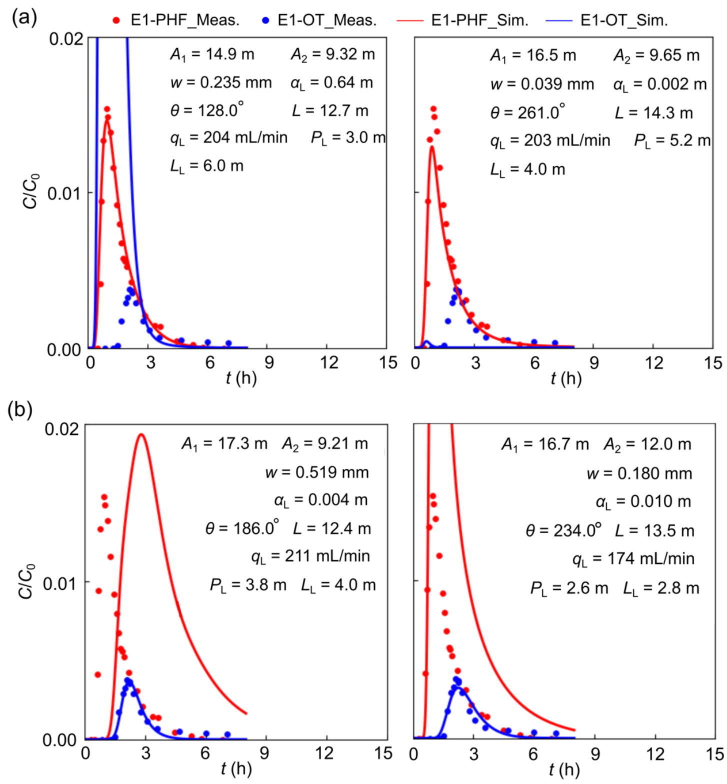

Fig. 12 Comparison between measured and simulated tracer breakthrough curves from the modeling of 31 October tracer test under the uniform aperture scenario. Only one tracer breakthrough curve is used for the modeling. (a) Tracer breakthrough curve at E1-PHF is used. (b) Tracer breakthrough curve at E1-OT is used.

It is worth mentioning that although some previous studies treated C-Dots as a conservative tracer (Hawkins et al., 2017b; Mattson et al., 2019b), sorption isotherm tests from the EGS Collab project indicated that C-Dots exhibited a Langmuir type sorption to crushed phyllite rocks, the host rock of the Collab Experiment 1 test bed (Neupane et al., 2020). The sorption of C-Dots to surrounding rock formations during the six tracer tests modeled in this study might have been a reason for the discrepancy between the water recovery ratio and the C-

Dots mass recovery ratio (Mattson et al., 2019), causing inevitable uncertainties in our stochastic modeling results.

7. Conclusion

In this study, we carried out stochastic modeling for six conservative tracer tests performed during a series of circulation and fracture stimulation experiments spanning nearly one month at the EGS Collab Experiment 1 testbed. Numerous realizations were performed to simulate tracer transport processes in a fracture network model. Realizations that successfully reproduce the measured tracer breakthrough curves were obtained to gain insight into the flow system as well as its evolution at the testbed.

The present study demonstrates the feasibility and efficacy of stochastic tracer modeling for the characterization of fractured reservoirs in subsurface. The results in this study provide important insights into the flow and transport characteristics in a hydraulically stimulated fracture network, including the critical parameters, interaction between hydraulic and natural fractures, as well as the evolution of flow and transport processes in the fracture network in response to various experiments. Such knowledge for a real-world reservoir can facilitate reservoir design and operation, improve reservoir thermal/hydraulic performance and mitigate potential environmental hazards.

Acknowledgments

This research was performed in support of the EGS Collab project; taking place in part at the Sanford Underground Research Facility in Lead, South Dakota. The assistance of the Sanford

Underground Research Facility and its personnel in providing physical access and general logistical and technical support is acknowledged. Support from the EGS Collab team is gratefully acknowledged. This work was supported by U.S. Department of Energy, Geothermal Technologies Office, and performed under the auspices of the U.S. Department of Energy by Lawrence Livermore National Laboratory under Contract DE-AC52-07NA27344. This document is LLNL report LLNL-JRNL-807241-DRAFT. All the geological/geophysical data of the EGS Collab Experiment 1, as well as the tracer test data in this study are publicly available through the U.S. Department of Energy's Geothermal Data Repository with a project number of EE0032708 (https://gdr.openei.org).

Appendix A. Supplementary data

Supplementary data associated with this article can be found in the online version.

References

Becker, M. W. & Shapiro, A. M. (2000). Tracer transport in fractured crystalline rock: Evidence of nondiffusive breakthrough tailing. *Water Resources Research*, *36*(7), 1677-1686. https://doi.org/10.1029/2000WR900080

Becker, M. W. & Shapiro, A. M. (2003). Interpreting tracer breakthrough tailing from different forced-gradient tracer experiment configurations in fractured bedrock. *Water Resources Research*, *39*(1), 1024. https://doi.org/10.1029/2001WR001190

Berkowitz, B. (2002). Characterizing flow and transport in fractured geological media: A review. *Advances in Water Resources*, *25*, 861-884. https://doi.org/10.1016/S0309-1708(02)00042-8

Bianchi, L., & Snow D. (1968). Permeability crystalline rock interpretated from measured orientations and apertures of fractures. *Annu. Arid Zone*, 8(2), 231-245.

Brasseur, G. P. & Jacob, D. J. (2017). Modeling of Atmospheric Chemistry. Cambridge University Press, Cambridge.

Bullivant, D. P. & O'Sullivan, M. J. (1989). Matching a field tracer test with some simple models. *Water Resources Research*, *25*(8), 1879-1891. https://doi.org/10.1029/WR025i008p01879

Brown, D. W., Duchane, D. V., Heiken, G. & Hriscu, V. T. (2012). *Mining the earth's heat: Hot dry rock geothermal energy*, Springer, Berlin.

Cacas, M. C., Ledoux, E., de Marsily, G., Barbreau, A., Calmels, P., Gaillard, B., et al. (1990a). Modeling fracture flow with a stochastic discrete fracture network: Calibration and validation: 2. The transport model. *Water Resources Research*, *26*(3), 491-500. https://doi.org/10.1029/WR026i003p00491

Cacas, M. C., Ledoux, E., de Marsily, G., Tillie, B., Barbreau, A., Durand, E., et al. (1990b). Modeling fracture flow with a stochastic discrete fracture network: Calibration and validation: 1. The flow model. *Water Resources Research*, *26*(3), 479-489. https://doi.org/10.1029/WR026i003p00479

Castagna, M. & Bellin A. (2009). A Bayesian approach for inversion of hydraulic tomographic data. *Water Resources Research*, *45*, W04410. https://doi.org/10.1029/2008WR007078

Cuss, R. J., Harrington, J. F., Noy, D. J., Sathar, S. & Norris, S. (2015). An experimental study of the flow of gas along synthetic faults of varying orientation to the stress field: Implications for performance assessment of radioactive waste disposal. *Journal of Geophysical Research: Solid Earth*, *120*, 3932-3945. https://doi.org/10.1002/2014JB011333

Dobson, P. F., & Salve, R. (2009). Underground reconnaissance and environmental monitoring related to geologic CO_2 sequestration studies at the DUSEL facility, Homestake Mine, South Dakota. LBNL-2858E, Lawrence Berkeley National Laboratory, Berkeley, CA.

Fu, P., Hao, Y., Walsh, S. D. C. & Carrigan C. R. (2016). Thermal drawdown-induced flow channeling in fractured geothermal reservoirs. *Rock Mechanics and Rock Engineering*, *49*, 1001-1024. https://doi.org/10.1007/s00603-015-0776-0

Fu, P., Settgast, R. R., Hao, Y., Morris, J. P. & Ryerson, F. J. (2017). The influence of hydraulic fracturing on carbon storage performance. *Journal of Geophysical Research: Solid Earth*, 122, 9931-9949. https://doi.org/10.1002/2017JB014942

Gale, J. E. (1987). Comparison of coupled fracture deformation and fluid flow models with direct measurements of fracture pore structure and stress-flow properties. In proceedings of 28th U.S. Symposium on Rock Mechanics, Tucson, AZ.

Geier, J. E., Lindgren G. A. & Tsang, C.-F. (2019). Simplified representative models for long-term flow and advective transport in fractured crystalline bedrock. *Hydrogeology Journal*, *27*, 595-614. https://doi.org/10.1007/s10040-018-1875-2

Goovaerts, P. (1997). *Geostatistics for Natural Resources Evaluation*, Oxford University Press, New York.

Guo, B., Fu, P., Hao, Y., Peters, C. A. & Carrigan, C. R. (2016). Thermal drawdown-induced flow channeling in a single fracture in EGS. *Geothermics*, *61*, 46-62. https://doi.org/10.1016/j.geothermics.2016.01.004

Hawkins, A. J., Becker, M. W. & Tester, J. W. (2018). Inert and adsorptive tracer tests for Field measurement of flow-wetted surface area. *Water Resources Research*, *54*, 5341-5358. https://doi.org/10.1029/2017WR021910

Hawkins, A. J., Becker, M. W. & Tsoflias, G. P. (2017a). Evaluation of inert tracers in a bedrock fracture using ground penetrating radar and thermal sensors. *Geothermics*, *67*, 86-94. https://doi.org/10.1016/j.geothermics.2017.01.006

Hawkins, A. J., Fox, D. B., Becker, M. W. & Tester, J. W. (2017b). Measurement and simulation of heat exchange in fractured bedrock using inert and thermally degrading tracer tests. *Water Resources Research*, *53*, 1210-1230. https://doi:10.1002/2016WR019617

Hecht-Méndez, J., Paly, M., Beck, M. & Bayer, P. (2013). Optimization of energy extraction for vertical closed-loop geothermal systems considering groundwater flow. *Energy*

Conversion and Management, *66*, 1-10. http://dx.doi.org/10.1016/j.enconman.2012.09.019

Hermans, T., Nguyen, F., Klepikova, M., Dassargues, A. & Caers, J. (2018). Uncertainty quantification of medium- term heat storage from short-term geophysical experiments using bayesian evidential learning. *Water Resources Research*, *54*, 2931–2948. https://doi.org/10.1002/ 2017WR022135

Hubbert, M. K. & Willis, D. G. (1957). Mechanics of hydraulic fracturing. Trans. Soc. Pet. Eng. AIME, 210, 153-163.

Jones, E., Oliphant T. & Peterson P. (2001). SciPy: Open source scientific tools for Python. Retrieved from http://www.scipy.org.

Juliusson, E. & Horne, R. N. (2013). Characterization of fractured reservoirs using tracer and flow-rate data. *Water Resources Research*, *49*, 2327-2342. https://doi.org/10.1002/wrcr.20220

Karmakar, S., Ghergut, J. & Sauter, M. (2016). Geothermics Early-flowback tracer signals for fracture characterization in an EGS developed in deep crystalline and sedimentary formations: a parametric study. *Geothermics*, *63*, 242-252. https://doi.org/10.1016/j.geothermics.2015.08.007

Kneafsey, T. J., Blankenship, D., Knox, H. A., Johnson, T. C., Ajo-Franklin, J. B., Schwering, P. C., et al. (2019). *EGS Collab project: Status and progress*. Paper presented at the 44th Workshop on Geothermal Reservoir Engineering, Stanford, CA.

Kneafsey, T. J., Blankenship, D., Dobson, P. F., Morris, J. P., White, M. D., Fu, P., et al. (2020). *The EGS Collab project: Learnings from Experiment 1*. Paper presented at the 45th Workshop on Geothermal Reservoir Engineering, Stanford, CA.

Leonard, B. P. (1979). A stable and accurate convective modelling procedure based on quadratic upstream interpolation. *Computer Methods in Applied Mechanics and Engineering*, *19*, 59-98. https://doi.org/10.1016/0045-7825(79)90034-3

Mack, M. G. & Warpinski, N. R. (2000). Mechanics of hydraulic fracturing. In M. J. Economides, K. G. Nolte (Eds.), *Reservoir Stimulation*. Chichester, UK: John Wiley & Sons Ltd.

Mattson, E. D., Neupane, G., Plummer, M. A., Hawkins, A. J. & Zhang, Y. (2019a). *Preliminary Collab fracture characterization results from flow and tracer testing efforts*. Paper presented at the 44th Workshop on Geothermal Reservoir Engineering, Stanford, CA.

Mattson, E. D., Neupane, G., Hawkins, A. J., Burghard, J., Ingraham, M., Plummer, M. A., and EGS Collab Team. (2019b). Fracture Tracer Injection Response to Pressure Perturbations at an Injection Well. *GRC Transactions, 43*, 371-379.

McClure, M. W. & Horne, R. N. (2014). An investigation of stimulation mechanisms in Enhanced Geothermal Systems. *International Journal of Rock Mechanics and Mining Sciences*, *72*, 242-260. https://doi.org/10.1016/j.ijrmms.2014.07.011

Middleton, R.S., Carey, J. W., Currier, R. P., Hyman, J. D., Kang, Q., Karra, S., et al. (2015). Shale gas and non-aqueous fracturing fluids: Opportunities and challenges for supercritical CO2. *Applied Energy*, *147*, 500-509. https://doi.org/10.1016/j.apenergy.2015.03.023

Moreno, L., Tsang, Y. W., Tsang, C.-F., Hale, F. V. & Neretnieks, I. (1988). Flow and tracer transport in a single fracture: A stochastic model and its relation to some field observations. *Water Resources Research*, *24*(12), 2033-2048. https://doi.org/10.1029/WR024i012p02033

Neuman, S. P. (2005). Trends, prospects and challenges in quantifying flow and transport through fractured rocks. *Hydrogeology Journal*, *13*(1), 124-147. https://doi.org/10.1007/s10040-004-0397-2

Neupane, G., Mattson, E. D., Plummer, M. A., Podgorney, R. K. & EGS Collab Team. (2020). *Results of multiple tracer injections into fractures in the EGS Collab testbed-1*. Paper presented at the 45th Workshop on Geothermal Reservoir Engineering, Stanford, CA.

Novakowski, K. S., Evans, G. V., Lever, D. A. & Raven, K. G. (1985). A field example of measuring hydrodynamic dispersion in a single fracture. *Water Resources Research*, *21*(8), 1165-1174. https://doi.org/10.1029/WR021i008p01165

Oldenburg, C. M., Dobson, P. F., Wu, Y., Cook, P. J., Kneafsey, T. J., Nakagawa, S., et al. (2017). *Overview of the kISMET project on intermediate-scale hydraulic fracturing in a deep mine*. Paper presented at the 51st U.S. Rock Mechanics/Geomechanics Symposium, San Francisco, CA.

Patankar, S. V. (1980). Numerical Heat Transfer and Fluid Flow. Hemisphere Publishing Corporation, Washington DC.

Ptak, T., Piepenbrink, M. & Martac, E. (2004). Tracer tests for the investigation of heterogeneous porous media and stochastic modelling of flow and transport-a review of some recent developments. *Journal of Hydrology*, *294*, 122-163. https://doi.org/10.1016/j.jhydrol.2004.01.020

Pyrak-Nolte, L. J., & Morris, J. P. (2000). Single fractures under normal stress: The relation between fracture specific stiffness and fluid flow. *International Journal of Rock Mechanics and Mining Sciences*, 37, 245-262. https://doi.org/10.1016/S1365-1609(99)00104-5

Radilla, G., Sausse, J., Sanjuan, B. & Fourar, M. (2012). Interpreting tracer tests in the enhanced geothermal system (EGS) of Soultz-sous-Forêts using the equivalent stratified medium approach. *Geothermics*, *44*, 43-51. http://dx.doi.org/10.1016/j.geothermics.2012.07.001

Settgast, R. R., Fu, P., Walsh, S. D. C., White, J. A., Annavarapu, C. & Ryerson, F. J. (2017). A fully coupled method for massively parallel simulation of hydraulically driven fractures in 3-dimensions. *International Journal for Numerical and Analytical Methods in Geomechanics*, *41*, 627-653. https://doi.org/10.1002/nag.2557

Sobol', I. M. (1993). Sensitivity analysis for nonlinear mathematical models. *Mathematical Models and Computer Exp*, *1*(4), 407-414. https:// doi.org/10.18287/0134-2452-2015-39-4-459-461

Sudicky, E. A. & Frind, E. O. (1984). Contaminant transport in fractured porous media: Analytical solution for a two-member decay chain in a single fracture. *Water Resources Research*, *20*(7), 1021-1029. https://doi.org/10.1029/WR020i007p01021

Sun, W., Durlofsky, L. J. (2017). A new data-space inversion procedure for efficient uncertainty quantification in subsurface flow problems. *Mathematical Geosciences*, 49(6), 679-715. https://doi.org/10.1007/s11004-016-9672-8

Sun, Y. & Buscheck, T. A. (2003). Analytical solutions for reactive transport of N-member radionuclide chains in a single fracture. *Journal of contaminant hydrology*, *63*, 695-712. https://doi.org/10.1016/S0169-7722(02)00181-X

Sun, Y. & Tong C. (2017). Dynamic reduced-order models of integrated physics- specific systems for carbon sequestration. *Geomechanics and Geophysics for Geo-Energy and Geo-Resources*, *3*(3), 315-325. https://doi.org/10.1007/s40948-017-0061-7

Tang, D. H., Frind, E. O. & Sudicky, E. A. (1981). Contaminant transport in fractured porous media: Analytical solution for a single fracture. *Water Resources Research*, *17*(3), 555-564. https://doi.org/10.1029/WR017i003p00555

Tsang, C.-F., Neretnieks, I. & Tsang, Y. (2015). Hydrologic issues associated with nuclear waste repositories. *Water Resources Research*, *51*, 6923-6972. https://doi.org/10.1002/2015WR017641

Tsang, Y. W., & Tsang, C. F. (1989). Flow channeling in a single fracture as a two-dimensional strongly heterogeneous permeable medium. *Water Resources Research*, 25(9), 2076-2080. https://doi.org/10.1029/WR025i009p02076

Tsang, Y. W., Tsang, C.-F., Hale, F. V. & Dverstorp, B. (1996). Tracer transport in a stochastic continuum model of fractured media. *Water Resources Research*, *32*(10), 3077-3092. https://doi.org/10.1029/96WR01397

U.S. Department of Energy. (2019). *GeoVision: Harnessing the Heat Beneath our Feet*. U.S. Department of Energy, Washington, D.C. https://www.energy.gov/eere/geothermal/geovision.

Vandenbohede, A., Lebbe, L. (2003). Combined interpretation of pumping and tracer tests: theoretical considerations and illustration with a field test. *Journal of Hydrology*, *277*, 134-149. https://doi.org/10.1016/S0022-1694(03)00090-8

Vogt, C., Kosack, C. & Marquart, G. (2012). Stochastic inversion of the tracer experiment of the enhanced geothermal system demonstration reservoir in Soultz-sous-Forêts — Revealing pathways and estimating permeability distribution. *Geothermics*, *42*, 1-12. https://doi.org/10.1016/j.geothermics.2011.11.001

Walsh, S. D. C., Carroll, S. A. (2013). Fracture-scale model of immiscible fluid flow. *Physical Review E*, *87*(1), 013012. https://doi.org/10.1103/PhysRevE.87.013012

Walsh, S. D. C., Du Frane, W. L., Mason, H. E., Carroll, S. A. (2013). Permeability of wellbore-cement fractures following degradation by carbonated brine. *Rock Mechanics and Rock Engineering*, *46*(3), 455-464. https://doi.org/10.1007/s00603-012-0336-9

White, M. D., Johnson, T. C., Kneafsey, T. J., Blankenship, D., Fu, P., Wu, H., et al. (2019). *The necessity for iteration in the application of numerical simulation to EGS:*

Examples from the EGS Collab test bed 1. Paper presented at the 44th Workshop on Geothermal Reservoir Engineering, Stanford, CA.

White, M. D., Fu, P., Ghassemi, A., Huang, H., Rutqvist, J., Johnston, B., et al. (2018). *Numerical Simulation Applications in the Design of EGS Collab Experiment 1*. Paper presented at the 43rd Workshop on Geothermal Reservoir Engineering, Stanford, CA.

Wu, H., Fu, P., Morris, J. P., Settgast, R. R., & Ryerson, F. J. (2019). ICAT: A numerical scheme to minimize numerical diffusion in advection-dispersion modeling and its application in identifying flow channeling. *Advances in Water Resources*, 134, 103434. https://doi.org/10.1016/j.advwatres.2019.103434

Zhang, Y., Dekas, A. E., Hawkins, A. J., Parada, A. E., Gorbatenko, O., Li, K., & Horne, R. N. (2019). Microbial community composition in deep-subsurface reservoir fluids reveals natural interwell connectivity. *Water Resources Research*, *55*. https://doi.org/10.1029/2019WR025916

Zhou, Q., Oldenburg, C. M., Kneafsey, T. J., and EGS Collab Team. (2018). *Modeling transport of multiple tracers in hydraulic fractures at the EGS Collab Test Site*. Paper presented at the 43rd Workshop on Geothermal Reservoir Engineering, Stanford, CA.